

7-2003

Study of Geometric Effects on Local Corrosion Rates for LBE Loop

Chao Wu

University of Nevada, Las Vegas

Follow this and additional works at: <https://digitalscholarship.unlv.edu/thesesdissertations>



Part of the [Mechanical Engineering Commons](#), [Mechanics of Materials Commons](#), and the [Nuclear Engineering Commons](#)

Repository Citation

Wu, Chao, "Study of Geometric Effects on Local Corrosion Rates for LBE Loop" (2003). *UNLV Theses, Dissertations, Professional Papers, and Capstones*. 1497.

<http://dx.doi.org/10.34917/3953046>

This Thesis is protected by copyright and/or related rights. It has been brought to you by Digital Scholarship@UNLV with permission from the rights-holder(s). You are free to use this Thesis in any way that is permitted by the copyright and related rights legislation that applies to your use. For other uses you need to obtain permission from the rights-holder(s) directly, unless additional rights are indicated by a Creative Commons license in the record and/or on the work itself.

This Thesis has been accepted for inclusion in UNLV Theses, Dissertations, Professional Papers, and Capstones by an authorized administrator of Digital Scholarship@UNLV. For more information, please contact digitalscholarship@unlv.edu.

STUDY OF GEOMETRY EFFECTS ON LOCAL CORROSION RATES
FOR LBE LOOP

by

Chao Wu

Bachelor of Science
Southeast University
2001

Master of Science
University of Nevada, Las Vegas
2003

A thesis submitted in partial fulfillment of
the requirement for the

Master of Science
Department of Mechanical Engineering
Howard R. Hughes College of Engineering

Graduate College
University of Nevada, Las Vegas
July 2003

ABSTRACT

Study of Geometry Effects on Local Corrosion Rates for LBE Loop

by

Chao Wu

Dr. Yitung Chen, Examination Committee Co-Chair
NCACM, Interim Director

Dr. Samir Moujaes, Examination Committee Co-Chair
UNLV, Associate Professor of Mechanical Engineering

Corrosion is an extremely important issue in nuclear cooling system applications. Many scientific and engineering efforts have been contributed to the research of finding an ideal material, which has resistance to corrosive Lead Bismuth Eutectic (LBE). A Delta Loop was designed and constructed in Los Alamos National Lab (LANL) to obtain the experimental data. This loop is a multi-section closed system that differs in diameter from one part to another. As a result, an intensive study on the geometry effect is hence necessary and valuable. In this thesis, this problem was simulated by commercial software STAR-CD. Results provide a good prediction where the highest corrosion rate might occur and how geometry will affect the local corrosion phenomenon. Simple study on reactive flow was carried out by using STAR-CD + CHEMKIN, which is designed for solving reactions both in flow and on surface. In addition, a self-developed code using finite difference method was employed to reveal how mass transfer is affected by geometry and flow. Parametric study on several factors was carried out.

TABLE OF CONTENTS

ABSTRACT.....	ii
LIST OF FIGURES.....	iv
ACKNOWLEDGEMENTS.....	vi
CHAPTER 1 INTRODUCTION.....	1
Nuclear Energy.....	1
Nuclear Waste.....	2
Transmutation Research Program.....	3
Materials Test Loop.....	4
Lead-Bismuth Eutectic.....	5
Purpose of Study.....	7
CHAPTER 2 PHYSICAL MODELS AND NUMERICAL METHODS.....	8
Part One: Self-developed Code.....	8
Part Two: Numerical Simulation using STAR-CD.....	13
CHAPTER 3 RESULTS AND DISCUSSIONS.....	20
Results from Self-developed Code and Discussions.....	20
Results from STAR-CD and Discussions.....	30
CHAPTER 4 CONCLUSIONS AND SUGGESTIONS.....	49
REFERENCES.....	51
VITA.....	55

LIST OF FIGURES

Figure 1.1 Materials Test Loop (LANL).....	5
Figure 2.1 Physical calculation domains.....	9
Figure 3.1 Streamlines for Reynolds numbers equal to 10 (a), 30 (b) and 150 (c).....	23
Figure 3.2 Comparison of expansion ratios vs. critical Reynolds numbers between current study and Drikakis [30].....	24
Figure 3.3 Concentration gradient vs. distance to inlet at expansion ratio of 10.....	26
Figure 3.4 Concentration gradient vs. distance to inlet at expansion ratio of 6.....	27
Figure 3.5 Concentration gradient vs. distance to inlet at expansion ratio of 3.....	28
Figure 3.6 Peak locations in axial direction for different expansion ratios.....	29
Figure 3.7 Concentration gradient vs. distance to inlet at different Schmidt number.....	30
Figure 3.8 Schematic of sudden expansion geometry.....	32
Figure 3.9 U-component of velocity of monitored cell at Re equal to 1000.....	33
Figure 3.10 Flow fluctuation.....	33
Figure 3.11 U-component of velocity of point one in different sizes of mesh.....	34
Figure 3.12 U-component of velocity of point two in different sizes of mesh.....	35
Figure 3.13 Mass transfer coefficient variation at Re=1,000.....	38
Figure 3.14 Mass transfer coefficient variation at Re=24,000.....	39
Figure 3.15 Mass transfer coefficient variation at Re=1,000.....	40
Figure 3.16 Mass transfer coefficient variation at Re=24,000.....	40

Figure 3.17 Geometric representation of the main test section in the MTL.....	42
Figure 3.18 Geometrical representation of an elbow section in the MTL.....	42
Figure 3.19 Velocity profiles of the fluids along the axial section of the pipe.....	43
Figure 3.20 Pressure variations along the axial section of the pipe.....	44
Figure 3.21 Variation of concentration of PbO along the axial pipe section.....	45
Figure 3.22 Closer view of the concentration variation of PbO.....	45
Figure 3.23 Velocity profile along the axial section of the elbow.....	46
Figure 3.24 Pressure profile along the axial section of the elbow.....	47
Figure 3.25 Concentration diagram of PbO along the surface of the elbow.....	47
Figure 3.26 Concentration profile of PbO along the axial section of the elbow.....	48

ACKNOWLEDGMENTS

This work is funded through the University of Nevada, Las Vegas, and Transmutation Research Program (TRP) University Participation Program administered by the Harry Reid Center for Environmental Studies (U.S. DOE Grant No. DE-FG04-2001AL67358). Supports and helps from Dr. Jinsuo Zhang, post-doctor at Los Alamos National Laboratory and Dr. Ning Li, program manager at Los Alamos National Laboratory are greatly appreciated.

I also want to give my gratitude to Dr. Yitung Chen, Dr. Samir Moujaes and Dr. Darrell Pepper, for the enlightening support and directions on my way of study and research.

CHAPTER I

INTRODUCTION

1.1 Nuclear Energy

Nowadays, nuclear energy supplies over 16% of the world's electricity, more than what the world used from all other sources in 1960. Today, totally, 31 countries are using nuclear energy to generate up to three quarters of their electricity, and a substantial number of these depend on it for one quarter to one half of their supply. Some 10,000 reactor years of operational experience have been accumulated since 1950s by the world's some 430 nuclear power reactors [1].

Nuclear energy applied to generating electricity is simply an efficient way of boiling water to make steam which drives turbine generators. Except for the reactor itself, a nuclear power station works like most coal or gas-fired power stations. Nuclear energy is best applied to medium and large-scale electricity generation on a continuous basis. The fuel for it is basically uranium.

Nuclear energy has distinct environmental advantages comparing to fossil fuels, in that virtually all its wastes are contained and managed. Nuclear power stations cause negligible pollution, if they are operated under controlled environment and condition. Furthermore the fuel for it is virtually unlimited, considering both geological and technological aspects. That is to say, there is plenty of uranium in the earth's crust and well-proven technology means that we can extract about 60 times as much energy from it

as we do today. The safety record of nuclear energy is better than for any major industrial technology.

Nuclear energy is drawing more and more attention across the world. Huge amount of funding and work is being invested on this important and beneficial topic.

1.2 Nuclear Waste

Fission occurs when atoms split and cause a nuclear reaction. Nuclear waste is produced whenever nuclear fission takes place and high-level radioactive waste is a by-product of making electricity at commercial nuclear power plants. It also comes from nuclear materials produced at defense facilities. Nuclear waste is predominately comprised of used fuel discharged from operating nuclear reactors [2].

Nuclear waste is a challenging problem people are facing, not only nationally, but also globally. In the United States, the roughly 100 operating reactors (which currently produce about 20% of the nation's electricity) will create about 87,000 tons of such discharged or "spent" fuel over the course of their lifetimes. Sixty thousand tons of this waste is destined for geologic disposal at the Yucca Mountain site in Nevada, along with another ~10,000 tons of so-called defense waste. Worldwide, more than 250,000 tons of spent fuel from reactors currently operating will require disposal.

These numbers account for only high-level radioactive nuclear waste generated by present-day power reactors. Nuclear power could develop so quickly by year 2050, that almost 1 million tons of discharged fuel - requiring disposal, could exist. All of these depend on how to handle the waste to improve the safety and environment concern [3].

1.3 Transmutation Research Program

Transmutation Research Program (TRP) is formerly known as “Advanced Accelerator Application” program (AAA). It involves the effort from universities by University Participation Program (UPP), which is a partnership between national laboratories and universities.

The TRP is improving the current nuclear waste processing technology; so that there is less concern over the management of the nuclear waste produced by nuclear power plants and developing a technology base for nuclear waste transmutation, which researchers hope can transform long-lived radioactive materials into short-lived or non-radioactive materials. Efforts are also being made to demonstrate its practicality and value for long-term waste management. The transmutation technology under study has the potential to extract energy from nuclear waste and make it available to the national power grid, representing a potentially huge amount of energy (equivalent to ~10 billion barrels of oil) [3].

The TRP also plans to construct an advanced accelerator-driven test facility that will provide unique and flexible capabilities for demonstration of nuclear waste transmutation and advanced nuclear technologies such as those for Generation IV reactors (solving electricity shortage and current electricity generation environmental contamination.).

Another troublesome issue is the decline of engineers or scientists with a nuclear background. Since 1980, nuclear engineering enrollments at US universities have sharply declined. No new nuclear power plants have been ordered in the United States since the late 1970s. Although the US retains considerable influence in global nuclear issues due to its superpower status, its relevance and leadership in the international arena of nuclear

technology is shrinking substantially. The TRP and its University Participation Program will establish and support a national university program to reenergize development and training in nuclear engineering and related fields, and develop research partnerships to rebuild a declining national nuclear science technology base.

The central theme and purpose of this program at UNLV is to involve students in research on the economically and environmentally sound refinement of spent nuclear fuel. The long-term goals of this program are to increase the University's research capabilities, attracting students and faculty of the highest caliber, while furthering the national program to address one of the nation's most pressing technological and environmental problems.

1.4 Materials Test Loop

Los Alamos National Laboratory's Accelerator-driven Transmutation of Waste (ATW) applications and the Department of Energy's TRP program have invested in developing Lead-Bismuth Eutectic (LBE) technology from spallation target and nuclear coolant applications since 1997. A Materials Test Loop (MTL) has been set up in Los Alamos.

The MTL is a facility designed to test the safe operation of a medium-size, forced circulation LBE system with representative thermal hydraulic conditions (as spallation target and/or transmutation blanket systems), to perform corrosion tests, and to develop candidate materials with oxygen control (and related probes and control systems).

It is a closed loop consisting of a pump, piping, heat exchangers and tanks. Figure 1 depicts more details. The LBE flow velocity in the test section is up to 3 m/s with a

volumetric flow rate up to $15 \text{ m}^3/\text{h}$. The maximum loop temperature is 500°C with a minimum temperature difference of 100°C along the loop. The design lifetime is estimated to be 3 years or more.

MTL is an essential part of the out-of-beam testing program in the U.S. MTL is a major step towards demonstrating the use of LBE on a scale representative of megawatts level spallation targets. Figure 1 shows the skeleton representation of the MTL.

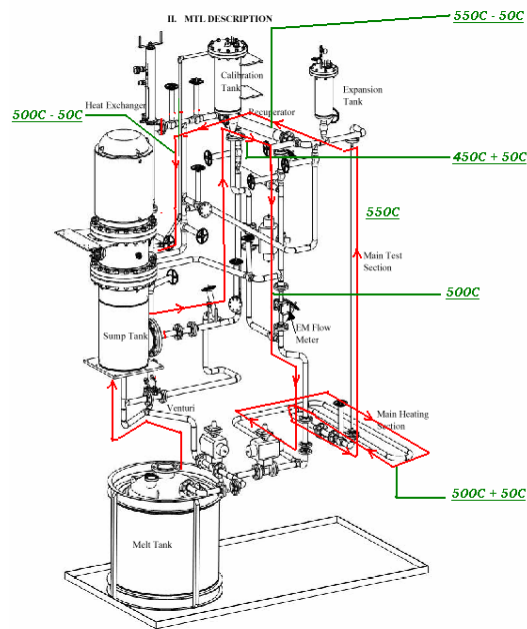


Figure 1.1 Materials Test Loop (LANL)

1.5 Lead-Bismuth Eutectic

The concept of a nuclear reactor using LBE as a coolant was considered in United States in the 1950's and it was put into practical use by Russians in submarine reactors [4].

LBE has exceptional chemical, thermal physical, nuclear and neutronic properties well suited for nuclear coolant and spallation target applications. In particular, LBE has a low melting temperature (123.5⁰C) and very high boiling temperature (~1670⁰C), is chemically inert and does not react with air and water violently, and can yield close to 30 neutrons per 1 GeV proton.

In recent years, LBE has received resurgent interest worldwide as a candidate for nuclear coolant applications in advanced reactors that are simple, modular, passively safe and proliferation resistant, with long-lasting fuels. However, corrosion caused by LBE has long been recognized as a leading obstacle to its nuclear applications and LBE has not been used in high-power spallation targets [5]. Liquid LBE alloy is known to be particularly aggressive towards iron and nickel, main components of stainless steels. The long-term reliability of piping containing LBE is determined by its resistance to being dissolved, eroded or corroded by the liquid.

One technique to solve this problem is to employ active oxygen control. The resistance to corrosion is greatly enhanced if a protective layer of oxide exists on the metal surfaces in contact with liquid. LBE is relatively inert compared to the metal components in steel [6]. Once Fe and Cr based oxides are formed on the steel surface; the dissolution of metal comes to a negligible level so that the loop is able to sustain a 2-3 year period that satisfies the design.

Tremendous effort has been made on the study of LBE and oxygen control technique. Gromov *et al.* presented the experience of using LBE coolant in reactors of Russian nuclear submarines and key results of developments for use of a LBE coolant in nuclear reactors and accelerator-driven systems [7]. Courouau *et al.* studied the different

specific methods to control the impurity of LBE, which is of major interest for ensuring adequate and safe operation of LBE facilities [8]. Soler Crespo *et al.* and Ning Li carried out experiments to examine the corrosion in LBE system in static and dynamic conditions [9] [10]. Balbaud-Célérier *et al.* set up theoretical models to predict the hydrodynamic effects on the corrosion of steels exposed to flowing liquid LBE [11].

1.6 Purpose of Study

An important purpose of study presented in this thesis is to use numerical simulation to explore the effects on species transport from complicated geometry and also, from different flow conditions. From aforementioned researches conducted by other people, it can be observed that the approach of numerical simulation is not paid enough attention to and carried out systematically for practical problems.

Geometry effects have a great influence on flow behavior and species transport. As a result, local corrosion rate close to geometry change varies significantly from classic estimation in regular and simple domain. The Delta Loop in Los Alamos National Lab (LANL) has different sections that differ in diameter from one to another. Sudden expansions and sudden contractions are expected to show great differences in the local corrosion rate. Consequently, prediction of how corrosion rate is distributed provides important information to material selecting and safety issue. According to the suggestions from LANL, an intensive study on the geometry effect is hence necessary and valuable.

CHAPTER II

PHYSICAL MODELS AND NUMERICAL METHODS

Numerical analysis in this thesis is divided into two parts. One is 2-D sudden expansion problem solved by using a FORTRAN code which is developed by author. The code is only applicable to laminar flow and species transport in relatively small Reynolds Number (Re). Also, different types of boundary conditions can be modeled easily in this code. The other part is 2-D and 3-D problems having similar geometry solved by using commercial software, STAR-CD, which is available in the market. STAR-CD has several turbulent models built inside so that higher Re and more complicated flow condition can be handled.

2.1 Part One: Self-developed Code

2.1.1 Physical Model

As shown in Figure 2.1, it is a 2-D sudden expanded domain. Height of inlet is defined as d , and D designates the distance between expanded panels. A fully developed channel flow was used as an inlet condition. In the present study, Re number is defined by the average inlet velocity and the upstream channel height. The length of the channel is 300 step heights, therefore the outflow gradients of the flow variables in the streamwise direction could be considered equal to zero. Governing equations are non-

dimensionalized. Certain boundary condition for species was chosen. It will be discussed later in Chapter III Results and Discussions.

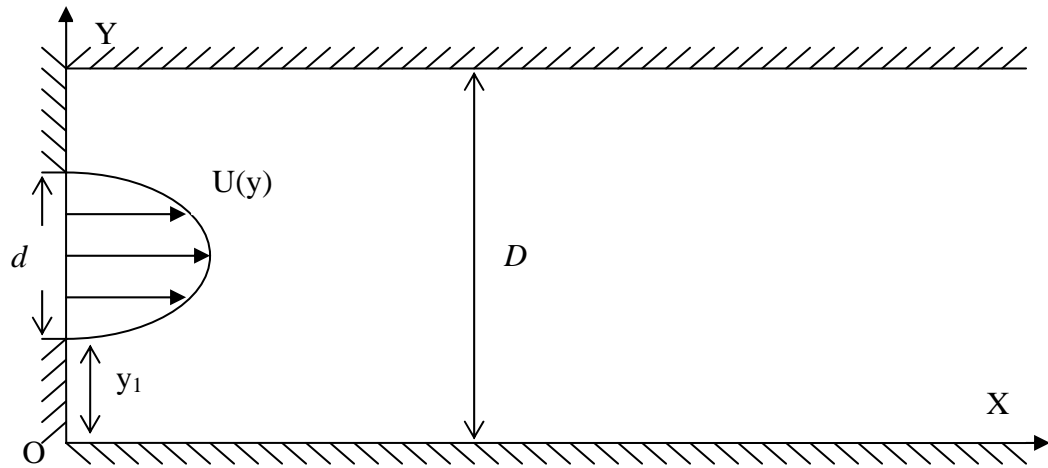


Figure 2.1 Physical calculation domains

2.1.2 Finite Difference Method

Finite Difference Method (FDM) modeling techniques were originally developed for human calculation efforts and the history of finite-difference calculations is very long.

FDM arises from the combination of two components:

- Differential equations of mathematical physics
- Replacement of differential operators with discrete difference approximations

Differential statements of the equations of mathematical physics are well known, as most of engineering and physics instruction is provided in this form. The analogous integral statement of this fundamental relation is more useful in computational practice. Because of this widespread knowledge of the differential form of standard equations for

modeling physical systems, the supply of differential equations that can be converted to analogous finite-difference schemes is essentially inexhaustible.

The computational component of finite-difference modeling arises from the replacement of the continuous differential operators with approximations based on discrete difference relations. The grid work of points where the discrete difference approximation is calculated is termed the finite-difference grid, and the collection of individual grid points used to approximate the differential operator is called the finite-difference molecule.

Finite-difference methods have many computational similarities to finite-element methods, but finite-difference models are less likely preserve any symmetry of the governing differential equations in the form of matrix symmetry. Finite-difference schemes possess several important computational advantages, among which is the fact that finite-difference models are very easy to implement for a wide variety of problems. In addition, finite-difference models are relatively simple to implement in software. While some real-world phenomena arise from engineering problems may compromise the utility of finite-difference approximations, such as irregular geometries, unusual boundary conditions and material dissimilarities [12].

2.1.3 Numerical Method

In the code, Finite-difference Method is applied. As mentioned before, the problem is treated non-dimensionally. Following reference scales for nondimensionalization are selected (See Figure 2.1):

- For the length: d , the width of inlet

- For the velocity: U_0 , the average flow velocity in d , $U_0 = \int U(y)dy / d$
- For the concentration: C_0 , the average concentration on the wall

The nondimensional parameters are:

- Reynolds Number: $Re = \frac{dU_0}{\nu}$
- Schmidt Number: $Sc = \frac{\nu}{D}$

We assume that the physical properties of the fluid are constant. Considering laminar incompressible flow, the 2-D Navier-Stokes equation in vorticity form is:

$$\frac{\partial \omega}{\partial t} + u \frac{\partial \omega}{\partial x} + v \frac{\partial \omega}{\partial y} = \nu \left(\frac{\partial^2 \omega}{\partial x^2} + \frac{\partial^2 \omega}{\partial y^2} \right) \quad (2.1)$$

where ν is equal to the reciprocal of Re , ω is vorticity and t is time.

Vorticity is defined to be equal to $\frac{\partial u}{\partial y} - \frac{\partial v}{\partial x}$.

The definition of stream function is:

$$u = \frac{\partial \psi}{\partial y} \quad v = -\frac{\partial \psi}{\partial x}$$

Substituting the definition of stream function into the incompressibility conditions ($\nabla \cdot U = 0$) leads to a Poisson Equation relating the stream function to vorticity.

$$\frac{\partial^2 \psi}{\partial x^2} + \frac{\partial^2 \psi}{\partial y^2} = \omega \quad (2.2)$$

In addition, Species Transport Equation (Equation. 2.3) is included.

$$\frac{\partial C}{\partial t} + u \frac{\partial C}{\partial x} + v \frac{\partial C}{\partial y} = a \left(\frac{\partial^2 C}{\partial x^2} + \frac{\partial^2 C}{\partial y^2} \right) \quad (2.3)$$

where a is reciprocal of Schmidt Number.

Equations 2.1-2.3 are governing equations solved in the code. After discretizing governing equations and applying first-order upwind formula to convection terms, Equations 2.4-2.6 are obtained and iterated by solver, which employs Successive Over-Relaxation (SOR) method. Various relaxation factors were tested and 1.5 was chosen to use.

$$\omega_{i,j}^{n+1} = \omega_{i,j}^n + \frac{\Delta t}{2\Delta x\Delta y} \left\{ \begin{array}{l} \left[\frac{2}{\text{Re}} \left(\frac{\Delta y}{\Delta x} \right) \left[\omega_{i+1,j}^n + \omega_{i-1,j}^n + \left(\frac{\Delta x}{\Delta y} \right)^2 (\omega_{i,j+1}^n + \omega_{i,j-1}^n) \right] \right. \\ \left. + \frac{1}{2} [(|u| - u)\omega_{i+1,j}^n + (|u| + u)\omega_{i-1,j}^n] \right. \\ \left. + \frac{1}{2} [(|v| - v)\omega_{i,j+1}^n + (|v| + v)\omega_{i,j-1}^n] \right. \\ \left. - \left[\frac{4\Delta y}{\text{Re}\Delta x} \left(1 + \frac{\Delta x^2}{\Delta y^2} \right) + |u| + |v| \right] \omega_{i,j}^n \right] \end{array} \right\} \quad (2.4)$$

$$2 \left[1 + \left(\frac{\Delta x}{\Delta y} \right)^2 \right] \psi_{i,j} = \psi_{i+1,j} + \psi_{i-1,j} + \left(\frac{\Delta x}{\Delta y} \right)^2 (\psi_{i,j+1} + \psi_{i,j-1}) - \Delta x^2 \omega_{i,j} \quad (2.5)$$

$$C_{i,j}^{n+1} = C_{i,j}^n + \frac{\Delta t}{2\Delta x\Delta y} \left\{ \begin{array}{l} \left[\frac{2}{\text{Sc}} \left(\frac{\Delta y}{\Delta x} \right) \left[C_{i+1,j}^n + C_{i-1,j}^n + \left(\frac{\Delta x}{\Delta y} \right)^2 (C_{i,j+1}^n + C_{i,j-1}^n) \right] \right. \\ \left. + \frac{1}{2} [(|u| - u)C_{i+1,j}^n + (|u| + u)C_{i-1,j}^n] \right. \\ \left. + \frac{1}{2} [(|v| - v)C_{i,j+1}^n + (|v| + v)C_{i,j-1}^n] \right. \\ \left. - \left[\frac{4\Delta y}{\text{Sc}\Delta x} \left(1 + \frac{\Delta x^2}{\Delta y^2} \right) + |u| + |v| \right] C_{i,j}^n \right] \end{array} \right\} \quad (2.6)$$

The inlet velocity of the fully developed flow is assigned to be:

$$U(y) = -6 * \left[\frac{(y - y_1)^2}{d^2} - \frac{y - y_1}{d} \right] \quad (2.7)$$

This is a parabolic function derived to fit the inlet and have zero velocity on both ends of inlet and maximum 1.5 at mid point of inlet.

According to the definition of stream function and vorticity, Corresponding inlet values of the stream function and vorticity are:

$$\psi(y) = \int U(y)dy = -6 * \left[\frac{(y - y_1)^3}{3d^2} - \frac{(y - y_1)^2}{2d} \right] \quad (2.8)$$

$$\omega(y) = \frac{dU}{dy} = \frac{6}{d} - \frac{12(y - y_1)}{d^2} \quad (2.9)$$

For the upper and bottom walls, non-slip boundary condition is imposed. Value for stream function of bottom wall is set to be zero, while upper wall has a constant stream function according to aforementioned integration. Expression for vorticity is

$$\omega_{wall} = \frac{\psi_{wall+1} - \psi_{wall}}{2\Delta n^2} \quad (2.10)$$

where Δn is the grid size in the direction normal to wall.

Treatment for outlet is straight forward.

$$\psi_{outlet} = \frac{4\psi_{outlet-1} - \psi_{outlet-2}}{3} \quad (2.11)$$

$$\omega_{outlet} = \frac{4\omega_{outlet-1} - \omega_{outlet-2}}{3} \quad (2.12)$$

$$C_{outlet} = 2C_{outlet-1} - C_{outlet-2} \quad (2.13)$$

2.2 Part Two: Numerical Simulation using STAR-CD

2.2.1 STAR-CD

Computer-aided analysis techniques have revolutionized engineering design in several important areas, notably in the field of structural analysis. Computational Fluid Dynamics (CFD) techniques are now exerting a similar influence on the analysis of fluid flow phenomena, including heat transfer, mass transfer and chemical reaction. The

frequent occurrence of such phenomena in industry and the environment has ensured that CFD is now a standard part of the Computer Aided Engineering (CAE) repertoire.

STAR-CD is a commercial, finite element based finite volume CFD code, developed by Computation Dynamics Limited. It is a powerful CFD tool for thermofluids analysis and has been designed for use in a CAE environment. Its many attributes include:

- A fully-integrated and user-friendly program suite comprising pre-processing, analysis and post-post-processing facilities
- A general geometry-modeling capability that renders the code applicable to the complex shapes often encountered in industrial applications
- Extensive facilities for automatic meshing of complex geometries, either through built-in tools or through interfaces to external mesh generators such as SAMMTM and ICEM CFD TetraTM
- Built-in models of an extensive and continually expanding range of flow phenomena, including transients, compressibility, turbulence, heat transfer, mass transfer, chemical reaction and multi-phase flow
- Fast and robust computer solution techniques that enhance reliability and reduce computing overheads
- Easy-to-use facilities for setting up and running very large CFD models using state-of-the-art parallel computing techniques
- Built-in links with popular proprietary CAD/CAE systems, including PATRANTM, IDEASTM and ANSYSTM

The STAR-CD system comprises the main analysis code, STAR (Simulation of Turbulent flow in Arbitrary Regions), and the pre-processor and post-processor code,

PROSTAR. A parallel-running version of the system, called STAR-HPC (High Performance Computing) is available as a separate product. Also separately available are two companion automatic-meshing packages, SAMM and ICEM CFD Tetra [13].

STAR-CD incorporates mathematical models of a wide range of thermofluid phenomena including steady and transient; laminar (non-Newtonian) and turbulent (from a choice of turbulence models); incompressible and compressible (transonic and supersonic); heat transfer (convection, conduction and radiation including conduction within solids); mass transfer and chemical reaction (combustion); porous media; multiple fluid streams and multiphase flow; body-fitted, unstructured, non-orthogonal; range of cell shapes, hexahedra, tetrahedra and prisms; embedded and arbitrary mesh; dynamic changes including distortion, sliding interface, and addition and deletion of cells during transient calculations.

The preprocessing and post-processing facilities of STAR-CD provide for all activities required to specify an application, perform the analysis and display and present the results. Some highlights are:

- Graphical user interface with both menu-driven and command-driven input facilities.
- Choice of expert mode accompanied by on-line error trapping, warning and helping facilities. Extensive mesh-generation tools, including embedded refinement and arbitrary mesh which allow user to handle complex geometry extremely quickly, offering various levels of automation according to problem complexity. Facilities for import and utilization of surface data in industry-standard IGES and VDA formats.

- Interfaces to proprietary CAD/CAE software for alternative geometry modeling, mesh generation, results display and other modes of analysis, including: ANSYSTM, ICEMTM, IDEASTM, NASTRANTM, and PATRANTM. Fast, efficient display techniques for mesh and results, geared to CFD requirement.
- Range of graphical display modes including vectors, contours, isosurfaces, particles tracks (static and dynamic), along with surface rendering.
- Freedom to view on arbitrary cutting planes and map solutions onto arbitrary meshes and surfaces. Animation facilities for dynamics portrayal of results.
- X-Y plotting facilities for quantitative display and comparison with external data.

2.2.2 Physical Model

Similar calculation domain to Figure 2.1 is built up using STAR-CD. Only difference is every parameter required by STAR-CD is dimensional and need to follow same unit system. Through powerful Graphic User Interface, properties of LBE are input into STAR-CD and structured mesh is generated. Different initial velocities and expansion ratios are used to do parametric study.

2.2.3 Numerical Method

The mass and momentum conservation equations solved by STAR-CD for general incompressible fluid flows and a moving coordinate frame (Navier-Stokes Equation) are, in Cartesian tensor notation:

$$\frac{1}{\sqrt{g}} \frac{\partial(\sqrt{g}\rho)}{\partial t} + \frac{\partial(\rho\tilde{u}_j)}{\partial x_j} = s_m \quad (2.14)$$

$$\frac{1}{\sqrt{g}} \frac{\partial(\sqrt{g}\rho u_i)}{\partial t} + \frac{\partial(\rho\tilde{u}_j u_i - \tau_{ij})}{\partial x_j} = -\frac{\partial p}{\partial x_i} + s_i \quad (2.15)$$

where t : time

x_i : Cartesian coordinate ($i=1,2,3$)

u_i : absolute fluid velocity component in direction x_i

\tilde{u}_j : $u_j - u_{cj}$, relative velocity between fluid and local (moving) coordinate frame that moves with velocity u_{cj}

p : piezometric pressure = $p_s - \rho_0 g_m x_m$, where p_s is static pressure, ρ_0 is reference density, the g_m are gravitational field components and the x_m are coordinates from a datum, where ρ_0 is defined

ρ : density

τ_{ij} : stress tensor components

s_m : mass source

s_i : momentum source components

\sqrt{g} : determinant of metric tensor

In case of laminar flows, STAR-CD caters for Newtonian fluids that obey the following constitutive relation:

$$\tau_{ij} = 2\mu s_{ij} - \frac{2}{3}\mu \frac{\partial u_k}{\partial x_k} \delta_{ij} \quad (2.16)$$

where μ is the molecular dynamic fluid viscosity and δ_{ij} , Kronecker delta, is unity when $i=j$ and zero otherwise. s_{ij} , the rate of strain tensor, is given by:

$$s_{ij} = \frac{1}{2} \left(\frac{\partial u_i}{\partial x_j} + \frac{\partial u_j}{\partial x_i} \right) \quad (2.17)$$

For turbulent flows, u_i , p and other dependent variables, including τ_{ij} , assume their ensemble averaged values (equivalent to time averages for steady-state situations) giving, for Equation 2.16:

$$\tau_{ij} = 2\mu s_{ij} - \frac{2}{3} \mu \frac{\partial u_k}{\partial x_k} \delta_{ij} - \overline{\rho u'_i u'_j} \quad (2.18)$$

where the u' are fluctuations about the ensemble average velocity and the over bar denotes the ensemble averaging process. The rightmost term in Equation 2.18 represents the additional Reynolds stresses due to turbulent motion. These are linked to the mean velocity field via the turbulence models.

A number of turbulence models are available in STAR-CD, such as $k - \varepsilon$ model and mixing-length model. The $k - \varepsilon$ turbulence model proposed by Harlow and Nakayama in 1968 is by far the most widely-used two-equation eddy-viscosity turbulence model, mainly because the epsilon was long believed to require no extra terms near walls. All the turbulent problems presented in this thesis were solved using $k - \varepsilon$ turbulence model.

As far as mass transfer is concerned, each constituent m of a fluid mixture, whose local concentration is expressed as a mass fraction m_m , is assumed to be governed by a species conservation equation of the form:

$$\frac{1}{\sqrt{g}} \frac{\partial(\sqrt{g} \rho m_m)}{\partial t} + \frac{\partial(\rho \tilde{u}_j m_m - F_{m,j})}{\partial x_j} = s_m \quad (2.19)$$

where $F_{m,j}$: diffusional flux component

s_m : rate of production or consumption due to chemical reaction

By analogy with the energy equation, laminar flow has

$$F_{m,j} \equiv \rho D_m \frac{\partial m_m}{\partial x_j} \quad (2.20)$$

where D_m is the molecular diffusivity of component m . While in case of turbulent flow,

$$F_{m,j} \equiv \rho D_m \frac{\partial m_m}{\partial x_j} - \overline{\rho u'_j m'_m} \quad (2.21)$$

where the rightmost term, containing the concentration fluctuation m'_m , represents the turbulent mass flux.

In some circumstances, it is not necessary to solve a differential conservation equation for every component of a mixture, due to the existence of algebraic relations between the species mass fractions. An example is the requirement of

$$\sum_m m_m = 1 \quad (2.22)$$

STAR-CD allows such relations to be exploited.

CHAPTER III

RESULTS AND DISCUSSIONS

In this chapter, results obtained from self-developed code and commercial package, STAR-CD, are presented. Various parameters were chosen to study the effects on mass transport. The study covers both of laminar and turbulent regions and shows valuable significance to practical applications.

3.1 Results from Self-developed Code and Discussions

3.1.1 Benchmark

Benchmark is important in research, especially in numerical simulation. It provides the validation of the tools and the base for the further effort. Before used to carry out calculation for more complicated cases, the code was applied to a classic problem and compare outcome with widely accepted results. Incompressible flow in sudden expansions is one of the classical problems and suits our calculation domain perfectly.

Studies of separated flows in plane sudden expansions were documented previously by several authors. Acrivos and Schrader [14], Milo and Acrivos [15] and Milos *et al.* [16] have conducted extensive numerical studies of plane and axisymmetric sudden expansion flows and investigated the existence of steady solution to the Navier-Stokes equations for both parabolic and uniform inlet velocity profiles. Acrivos and Schrader [14] carried out computations, on the basis of boundary layer equations, for several expansion ratios, and

found that steady solutions exist for all values of the parameter λ , the ratio of the inlet channel half-width to the step height, when the inlet profile is parabolic. Milos and Acrivos [15] carried out computations for a uniform inlet profile and several sudden expansion ratios. They used a global Newton method in order to circumvent the difficulties associated with the physical instability of the flow and their calculations revealed that the steady solution exists only if λ is below a critical value λ_c . Milos *et al.* [16] presented detailed computations of the Navier-Stokes equations up to a Reynolds number of 1000 (based on the step height) for a uniform inflow past a cascade of sudden expansions. Their calculations revealed that for large values of the expansions ratio the eddy length increases linearly with Re, while for smaller values of the expansion ratio the solution of the Navier-Stokes equations, with increasing Re, approaches an asymptotic state for the eddy length.

Experimental and numerical results for axisymmetric, incompressible sudden expansion flows have been presented by Macagno and Hung [17] at Reynolds numbers up to 200. Kwon *et al.* [18] and Kumar and Yajnik [19] studied numerically sudden expansion flows using the boundary-layer equations while Navier-Stokes calculations for symmetric flows past a sudden expansion have also been reported by Hung [20] and Morihara [21], and more recently by Scott *et al.* [22], Napolitano and Cinnela *et al.* [23], and Hawken *et al.* [24]. Recently, Baloch *et al.* [25] have also conducted a numerical study of two- and three-dimensional expansion flows based on the Navier-Stokes equations and a semi-implicit Taylor-Galerkin/pressure-correction finite element scheme, but the computations were limited to very low Reynolds numbers and no attempt was made to calculate flow bifurcations.

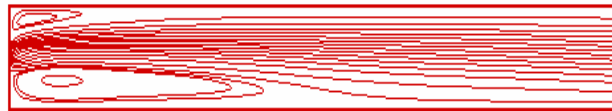
Early experimental studies by Durst *et al.* [26] of low Reynolds number flows over 1:2 and 1:3 plane expansions revealed asymmetric separation beyond a certain Reynolds number. The ratios mentioned in this thesis are the height of inlet to the height of expanded area. A further experimental study of flow in the same geometries was performed by Chedron *et al.* [27], demonstrating that symmetric flow in symmetric sudden expansions can exist only within a limited range of Reynolds numbers. Chedron *et al.* performed flow visualization in order to obtain time-averaged information about the various flow regimes near the sudden expansion. Under the conditions of an expansion ratio of 1:2 and grid aspect ratio of 8, they observed that the flow became asymmetric at Reynolds numbers higher than 185 based on the maximum velocity and upstream channel height. Another experimental and numerical study of the flow in symmetric sudden expansion, with expansion ratio 1:3, was published by Fearn *et al.* [28]. Their results were verified by Shapira *et al.* [29], who performed a linear stability analysis of symmetric flow in plane sudden expansions. Shapira *et al.* found a critical Reynolds number Re_c of 82.6 (based on the maximum velocity and upstream channel height), which is in good agreement with the results of Fearn *et al.* for an expansion ratio of 1:3 (Fearn *et al.* reported $Re_c=40.45$ based on the upstream channel half-height, i.e. $Re_c=80.9$ based on the upstream channel height.) Drikakis [30] numerically studied this sudden expansion problem and performed computations at various Reynolds number and expansion ratio, which turns out to be a good reference to compare with.

Figure 3.1 shows different flow behaviors according to different Reynolds numbers at expansion ratio of 1:6. When Reynolds number is low, flow develops symmetrically. While the increase of Reynolds number to certain point, symmetry is broken and

bifurcation is observed. In this case, this critical Reynolds number turns out to be 25. Finally, Reynolds number is getting too big for flow to keep steady. More vortexes are generated from corner and spread to downstream along the wall.



(a)



(b)



(c)

Figure 3.1 Streamlines for Reynolds numbers equal to 10 (a), 30 (b) and 150 (c)

It should be noted that the third picture in Figure 3.1 is distorted to give a better visual effect in limited space. The size of vortexes and the position of them are different from what and where they appear to be.

Similarly, more expansion ratios were considered. Different critical Reynolds numbers were obtained to benchmark with published results [30]. Figure 3.2 depicts how the curves of critical Reynolds number obtained from both self-developed code and

published results look like along expansion ratio. Drikakis [30] used maximum velocity of fully developed flow in the definition of Reynolds number, while average velocity was chosen in self-developed code. In light of this discrepancy, conversion has been done to Reynolds number so that the values from two sources are comparable. As can be seen from figure, two curves are very close to each other and the maximum of relative error is around 10%. Considering different numerical methods and order of accuracies involved, the results from self-developed code are reasonable and credible.

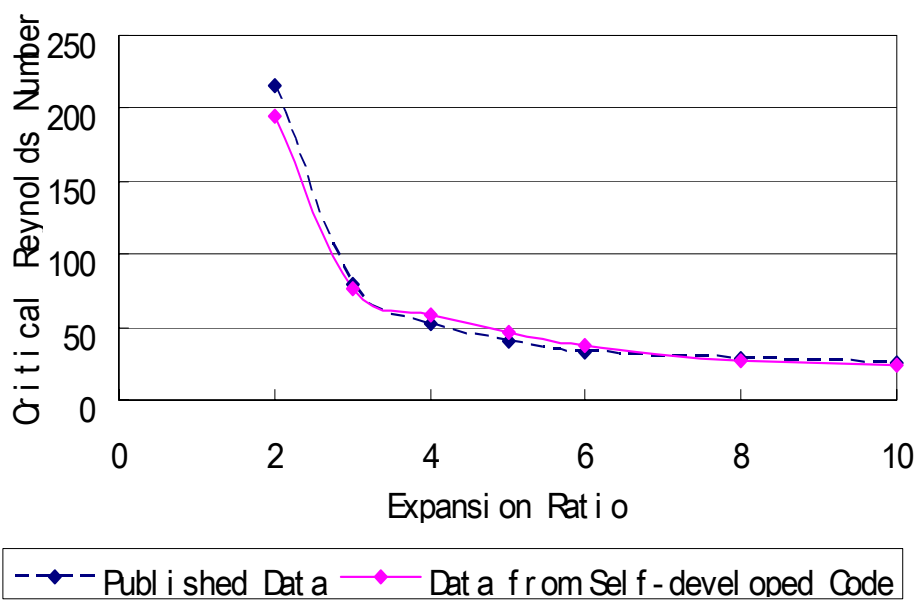


Figure 3.2 Comparison of expansion ratios vs. critical Reynolds numbers between current study and Drikakis [30]

3.1.2 Results from Self-developed Code and Discussions

In practical problem, corrosion takes place on the inner surface of loop. He *et al.* [31] published an empirical formula to prove that contaminants generated are function of local

temperature and the concentration of reactants. In the code, temperature was not taken account of. Then, uniform concentration of species was assumed as boundary condition at wall. In this way, continuous generated species whose movement is greatly affected by flow are modeled. As the products of corrosion, species move under both effects of diffusion and convection. The code reveals these complicated phenomena by solving governing equations aforementioned.

A numbers of factors affect mass transfer and corrosion rate by varying concentration gradient, especially when corrosion happens in the environment which involved complicated flow movement. Because of the truth that complicate flow situations always take place in the region close to corner and wall in this kind of sudden expansion geometry, the concentration gradient on the wall surface is of more importance than that in bulk region. Vortexes and circulations disturb the formation of boundary layer. Consequently, theoretical estimation of mass transfer phenomenon is not applicable and more uncertainties need to be considered in those kinds of situations. Flow pattern decides the way how species is washed from the wall and diffuses into bulk region. In the code, concentration gradient at wall is calculated according to expression $\frac{C_{wall} - C_{wall-1}}{\Delta y}$.

In the light of unsteady nature of flow, at each cross section, concentration gradients on upper and bottom wall are taken average to show general idea of how species is transported at near-wall region along the distance to inlet.

Work is basically carried out with the parametric study of several factors, such as Reynolds Number, expansion ratio and Schmidt Number. Different combinations show how those factors affect species transfer.

3.1.2.1 Expansion Ratio

To find out the effects on mass transfer brought in by expansion ratio, three ratios were chosen to look at. They are 3, 6 and 10. Figure 3.3, 3.4 and 3.5 show the concentration gradients at different Reynolds Number at each expansion ratio versus distance to inlet. The results are obtained after certain amount time elapses. They are results at one instance, not averaged over time.

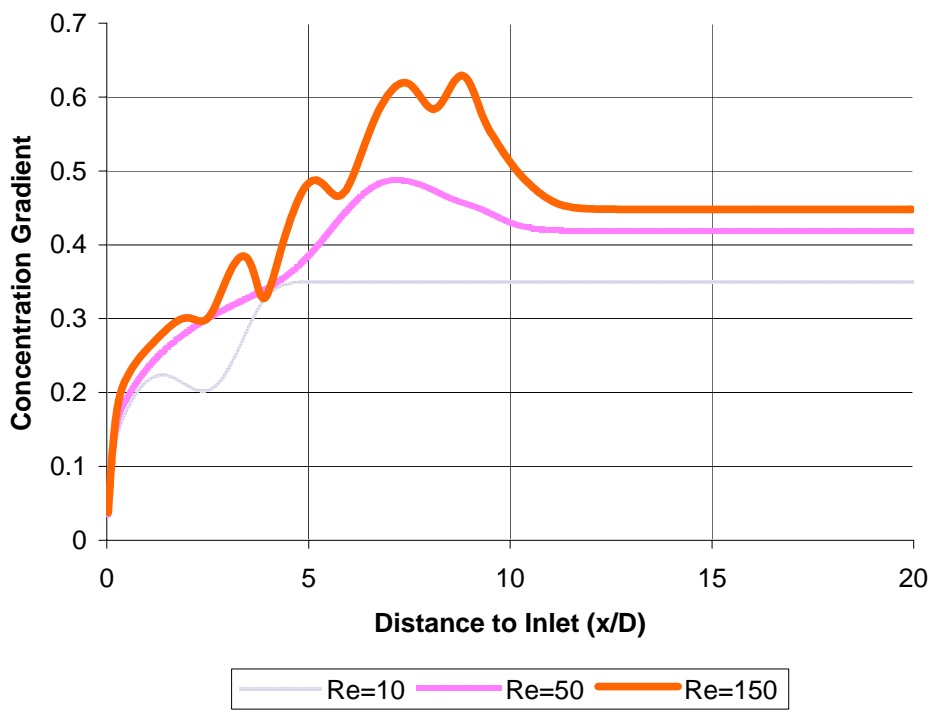


Figure 3.3 Concentration gradient vs. distance to inlet at expansion ratio of 10

From those figures, we can tell that, at each expansion ratio, higher Reynolds Number generally yields higher concentration gradient. When Reynolds Number is very low, like around 10, concentration gradient varies smoothly from inlet to a certain distance and reaches its maximum value. After that point, it remains at the same value. While Reynolds Number goes up, flow becomes unsteady. Instead of smooth curve, lines start

oscillating and contain numbers of peaks along x coordinate. It is because of vortexes and circulations disturb the formation of boundary layer. In near wall region, each recirculation zone affects mass transfer to a similar pattern, which is the reason why figures show several peaks with the shape close to each other. The difference between each of those oscillations in value and width is brought in by upstream which varies from

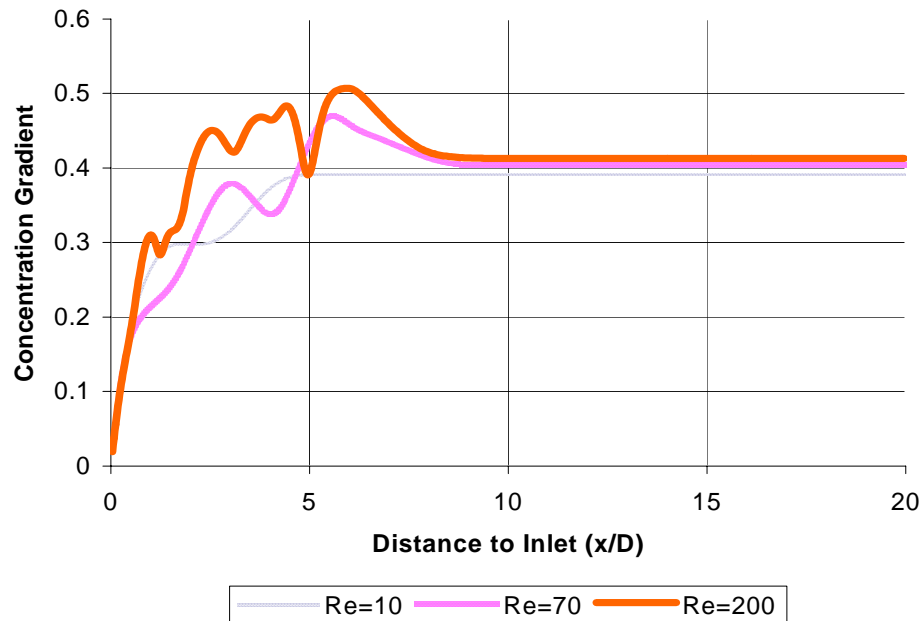


Figure 3.4 Concentration gradient vs. distance to inlet at expansion ratio of 6

one to another. One thing need to be noticed is, even though, concentration gradient lines of higher Reynolds Number in those figures seem to reach a steady situation, it is believed due to the inadequate computational time. Given more time steps, vortexes and circulations will spread to downstream along the wall. Time step is calculated according to $0.01 * \Delta x * \Delta y$, as suggested.

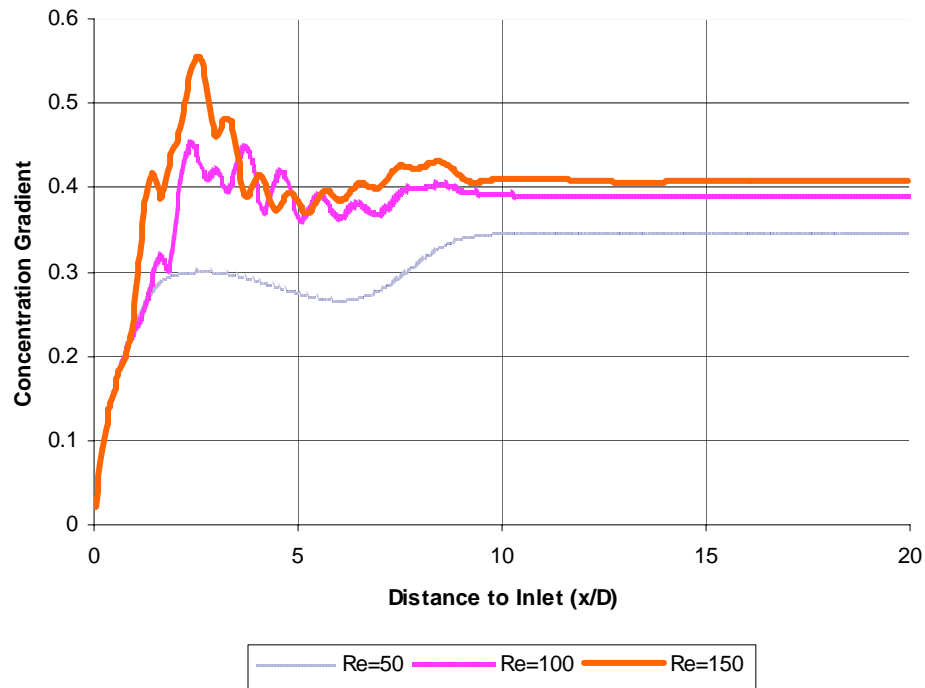


Figure 3.5 Concentration gradient vs. distance to inlet at expansion ratio of 3

It is also can be observed that for the same expansion ratio, maximum of concentration gradient for those relatively high Reynolds Numbers occurs almost at same distance to inlet, while the value of maximum differs in the same order. With the increasing of expansion ratio, the distance to inlet where biggest concentration gradient occurs is pushed downstream. Figure 3.6 depicts the trend between peak location and expansion ratio.

It can be concluded that, at same expansion ratio, higher Reynolds Number will bring higher concentration gradient so that corrosion will be more likely to happen. As far as expansion ratio, it will not change the scale of concentration gradient too much, but the place where maximum gradient occurs. Figure 3.6 reveals that the location of greatest gradient increases when expansion ratio becomes bigger.

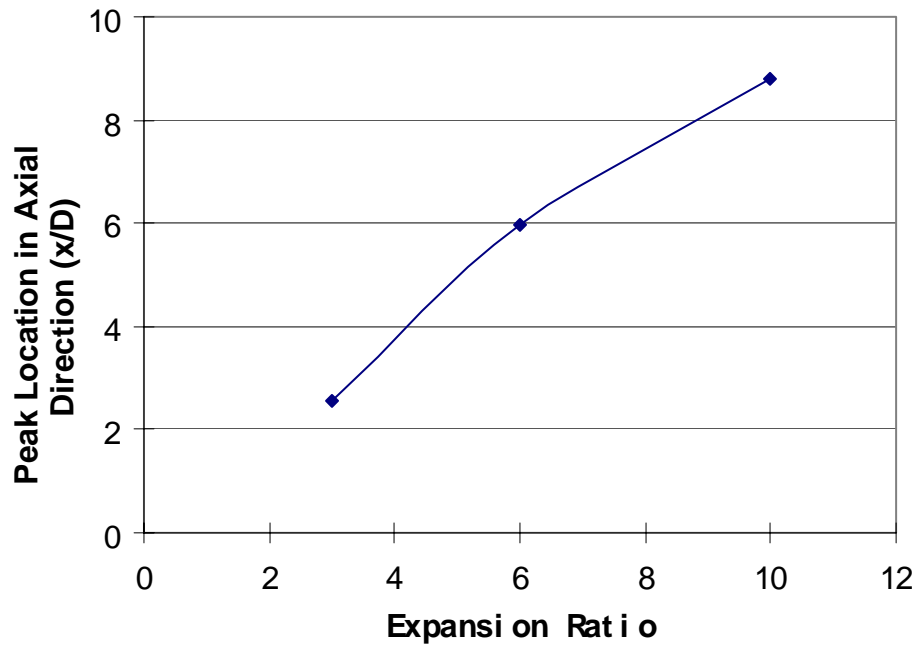


Figure 3.6 Peak locations in axial direction for different expansion ratios

3.1.2.2 Schmidt Number

From the definition given before, Schmidt number is equal to $\frac{\nu}{D}$, which is the ratio of viscosity and diffusivity. The value of Schmidt number affects mass transport significantly. So, parametric study on Schmidt number was also carried out.

In Figure 3.7, three curves represent concentration gradient variation along the distance to inlet at same Reynolds number of 150 and expansion ratio of 10 but different Schmidt numbers. As we can easily observe, higher Schmidt number yields higher concentration gradient. It is harder for species to diffuse inside to the bulk region than to be washed away by flow. As a result, the lower the Schmidt Number is, the less corrosion will happen, according to the scale of concentration gradient.

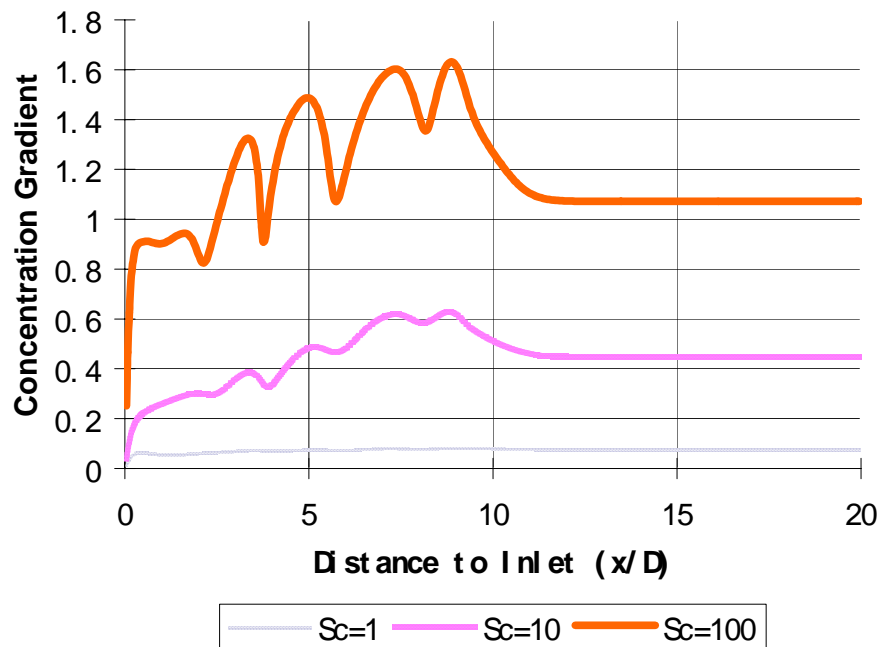


Figure 3.7 Concentration gradient vs. distance to inlet at different Schmidt number

3.2 Results from STAR-CD and Discussions

STAR-CD has been chosen as the CFD tools for analyzing fluid flow and species transportation. The method of solution used in STAR-CD is a Control Volume Method. The governing equations solved by STAR-CD for fluid analysis and mass transfer are shown below.

Continuity Equation:

$$\nabla \cdot \rho V = 0 \quad (3.1)$$

Momentum Equation:

$$\rho \frac{DV}{Dt} = \rho g - \nabla p + \mu \nabla^2 V \quad (3.2)$$

Energy Equation:

$$\rho C_p \frac{DT}{Dt} = k \nabla^2 T + \mu \Phi_v \quad (3.3)$$

Species Transport Equation:

$$\frac{DC}{Dt} = D_{coeff} \nabla^2 C + R \quad (3.4)$$

3.2.1 Model Setup

Study was carried out in 2-D models at this early stage. As shown in Figure 3.8, studied problem was given sudden expanded geometry. Temperature along the length of the plate is assumed constant. A uniformly generated mesh is used, which means the length and height are divided into equally spaced grids. Different mesh sizes were tested to check the mesh independence. Results on these tests are included later. Initially, flow does not contain any species at inlet, while two plates have a fixed concentration of species. In this way the species on the plates will diffuse into the bulk region, and the expected corrosion rate along the length may vary due to the difference of local flow condition and concentration profiles normal to the wall. Engineering unit here for the model is not important. Dimensionless scale is used in Figure 3.8. Inlet height, d , is 0.5, the height of expanded area is 1.0 and the length is 10. C_{wall} is set at 0.5 for both plates.

LBE is allowed to flow from inlet. All the physical properties of flow are listed in Table 3.1.

Meanwhile, it has been well accepted that Hopf bifurcation occurs in this kind of symmetric sudden expansion domain, when Reynolds number reaches certain critical value [32]. Oscillation or vibration appears in the flow and the resultant flow becomes unsteady and periodic in time. To verify that, one monitoring cell was assigned at

location (d, d) , according to Figure 3.8. Figure 3.9 proves that U-Component of velocity at monitoring cell oscillates and shows a periodic pattern. In addition, Figure 3.10 gives a direct idea how flow propagates along time. All those data and results are from the flow whose Reynolds number is equal to 1000.

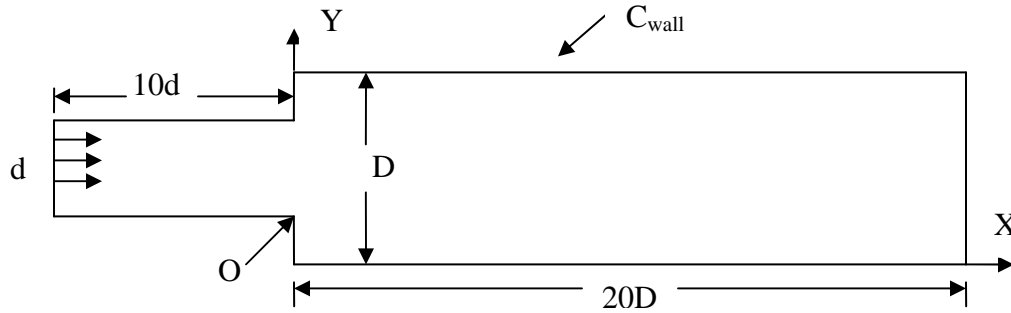


Figure 3.8 Schematic of sudden expansion geometry

Table 3.1 Physical Properties Used in Study

	Magnitude
Density	10120.3 kg/m^3
Molecular Viscosity	0.003941 kg/ms
Diffusivity	$10^{-9} \text{ m}^2/\text{s}$
Schmidt Number	389

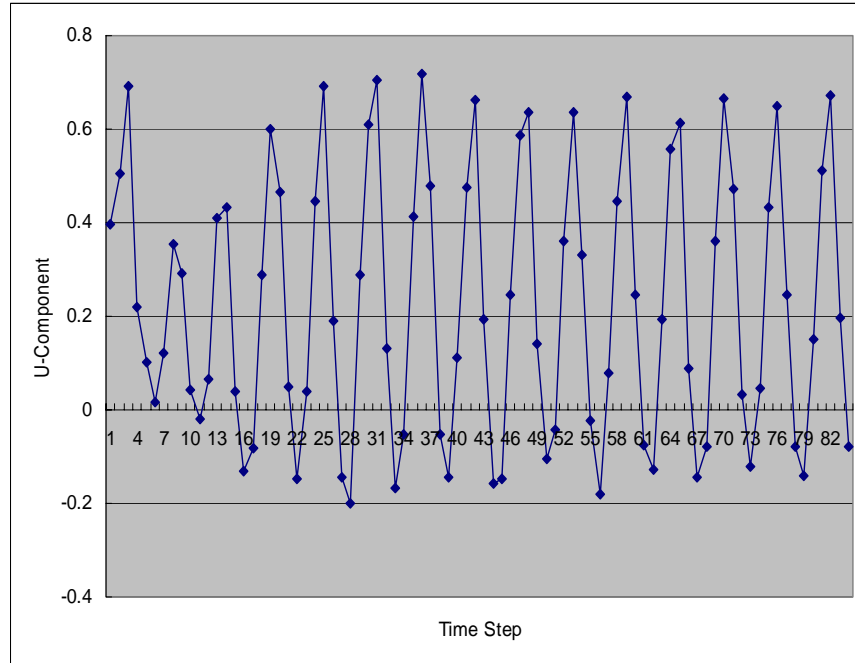


Figure 3.9 U-component of velocity of monitored cell at Re equal to 1000

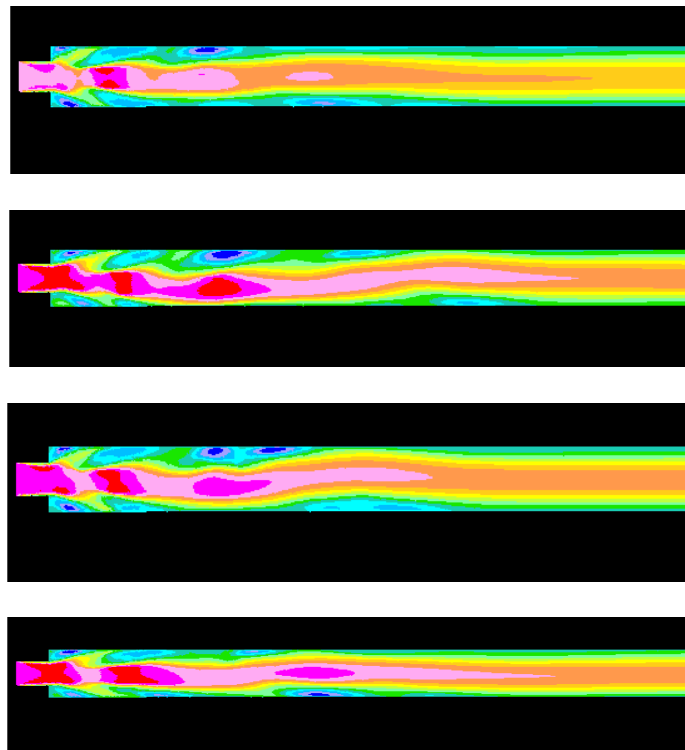


Figure 3.10 Flow fluctuation

3.2.2 Mesh Independence

Mesh independence is a crucial step for numerical simulation. It guarantees code and algorithm to produce as accurate results as it can and, at the same time, removes errors brought in by using different mesh sizes. A grid sensitivity study was performed using three grids: 400*100, 600*150 and 800*200.

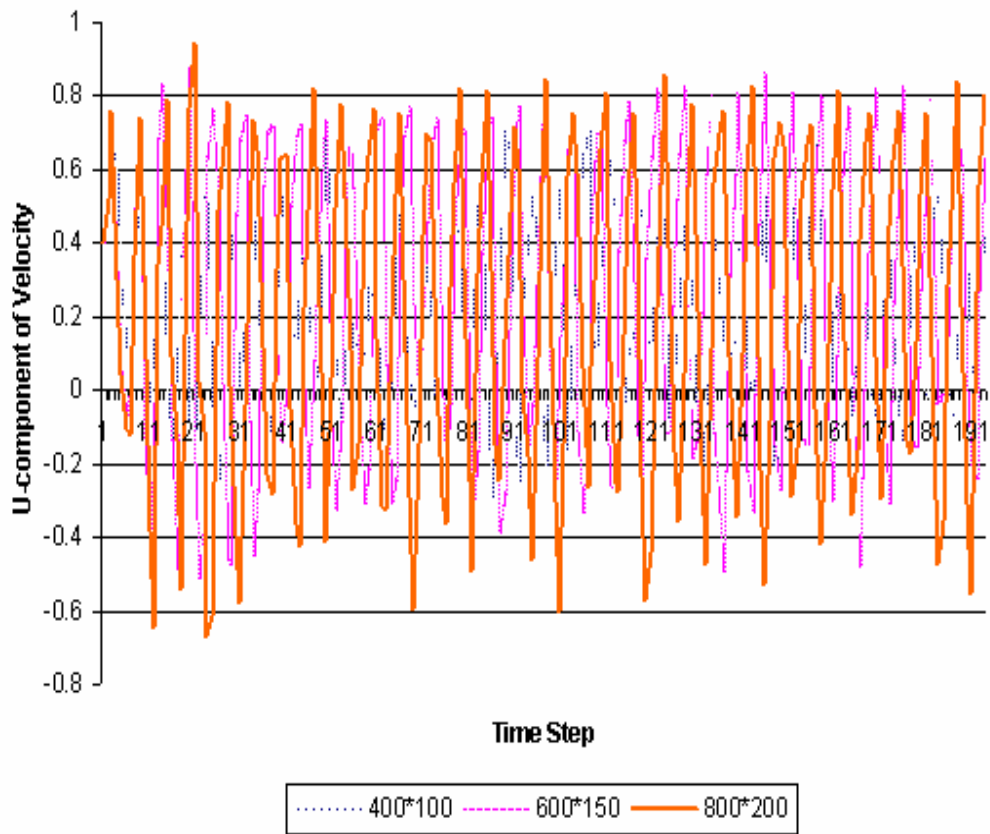


Figure 3.11 U-component of velocity of point one in different sizes of mesh

The geometry of testing model is same as before, a 2-D sudden expansion with ratio of 1:2. Reynolds Number is chosen as 1000. And, two points with coordinates (0.75, 0.5) and (1.0, 0.5) are picked as monitoring spots in each mesh size. To save calculation time,

only part of domain, which is four times of expanded diameter long in axial direction starting from expansion, is revised by giving different mesh sizes.

Results from three mesh sizes are presented in Figure 3.11 and Figure 3.12. Again, U-component of velocity was monitored to plot the variation over time step.

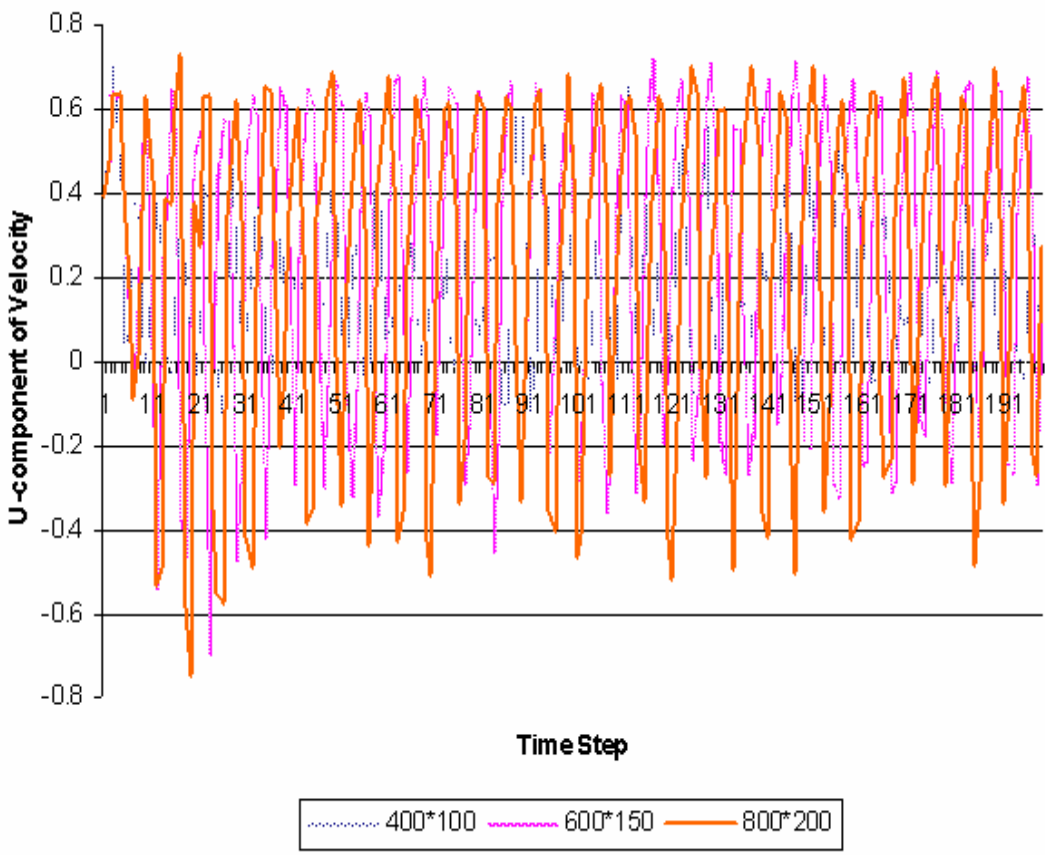


Figure 3.12 U-component of velocity of point two in different sizes of mesh

From two figures, the blue line, which stands for coarsest mesh, 400*100, is obviously far from the other two. While pink and yellow lines are quite close to each other. Both of them captured similar fluctuation. The phase of wave almost keeps oscillating in an identical way. The values at each time step are fairly close as well. After

the analysis of results in aforementioned three mesh sizes, the one with medium mesh density, e.g. 600*150, was selected to be used for further study. In this way, credibility of results can be ensured very well without paying too much computational time for higher fineness of mesh.

To answer the question why there is a noticeable difference between pink and yellow curves, the reason is the Reynolds number. With the increase of Reynolds number, flow becomes more unsteady and fluctuates more dramatically. In the results showed above, Reynolds number 1000 was employed. It is a relatively high, even though it is still in laminar region. For this kind of flow, it is much harder to bring the discrepancy among different mesh sizes down to negligible level. Considering these aspects, the medium mesh size is taken acceptable.

3.2.3 Results and Discussions

3.2.3.1 Mass Transfer Coefficient

Mass transfer coefficient, k , is the parameter used to measure mass transport phenomenon. In this case, it can be defined as:

$$k = \frac{D_{coeff} \cdot \Delta C}{\Delta y \cdot C_{wall}} \quad (3.5)$$

where ΔC is the concentration difference between wall and the first cell next to the wall, and Δy is half height of that cell, since value of parameters in finite volume method is calculated at center of each cell, instead of each node in other methods.

From Equation 3.5, mass transfer coefficient can be obtained at given x location. Data collected from different locations is plotted to reveal how mass transport is changed in axial direction by geometrical difference.

Due to the periodic nature of the flow at high Reynolds numbers, mass transfer coefficient at every location is time-averaged, which means data of each point are collected at several times on both of upper and bottom wall within one period and then taken average. This guarantees results more accurate in a long time scope and smoothes out some misleading information brought in by instability.

After geometry was set up, physical properties were assigned and boundary conditions were given, a model is ready to study on the mass transfer coefficient variation along the distance to expansion inlet. STAR-CD does not have built-in function to calculate mass transfer coefficient automatically. The raw data was extracted from STAR-CD and analyzed and plotted manually. STAR-CD has a limit for the number of values you can edit at same time, which is 1,000. Since each layer of nodes in x direction exceeds this number, data from first ten times of expanded diameter (10D) starting from expansion inlet were collected for the convenience.

Two Reynolds numbers, 1,000 and 24,000, were chosen to use. Consequently, both of laminar and turbulent flow is covered in the study. It can be observed that mass transfer coefficient varies with the distance after sudden expansion.

Two ways of averaging data over time were considered. The first way used is to separate the layer of cells which are next to walls, both of upper wall and bottom wall, at certain one time step and then get the concentration value of each of those cells. By doing this, we can subtract the value at each cell from the concentration at wall, which is uniform in this case, and get the ΔC . Easily, mass transfer coefficient in axial direction is obtained at upper and bottom walls, according to Equation 3.5. Average the pair of values having same x coordinates and get the mass transfer coefficients at one time step.

Repeating doing this at different time steps gives multiple sets of data. Finally, take the average out of those sets of data. The final values are considered time-averaged. Figure 3.13 and 3.14 show the output using this method. The drawback of this method is time-consuming work and low efficiency, which prevent a more accurate estimation. Results in Figure 3.13 and 3.14 are the averaged ten different time steps.

Figure 3.13 is mass transfer coefficient plotted at Reynolds number of 1,000. It reaches peak from starting value very quickly at around 1D and then decreases to smaller numbers at a nearly fixed slope. The peak value at 1D is almost four times of minimum. And the coefficient remains at a high level in the region close to expansion.

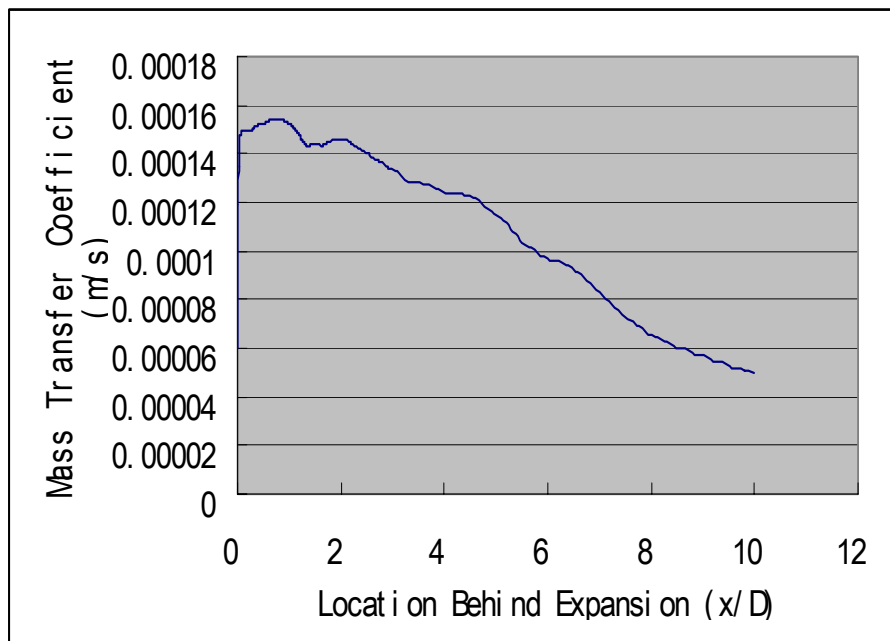


Figure 3.13 Mass transfer coefficient variation at $Re=1,000$

Figure 3.14 is obtained when Reynolds number at 24,000. High velocity flow enhances the species transfer. Comparing to Reynolds number of 1,000, coefficient values are approximately twice higher. However, the complicated nature of turbulent

flow makes mass transfer more instable and unpredictable. Vortexes and reattachments can greatly intensify local species transfer, due to higher velocity in those circulation zones. At such a high Reynolds number, locations of vortexes and reattachments are constantly moving with the propagation of flow which gives rise to the irregularity. Similar to laminar case, the region close to expansion, from 0 to 2D, has largest values in the whole domain. Mass transfer rate tends to decline, though there are a couple of sub-peaks in downstream.

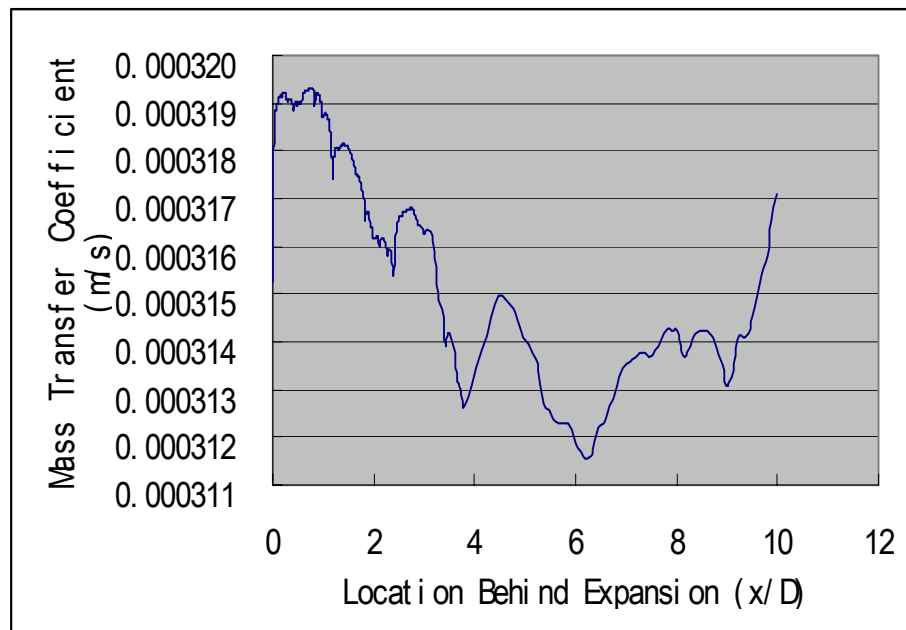


Figure 3.14 Mass transfer coefficient variation at $Re=24,000$

The second idea on how to average data is gotten from experiment, which uses electronic sensors to collect data over a time range. Similarly, twenty cells at locations of interest were saved in a .set file in STAR-CD. With cell monitoring feature in STAR-CD, concentration values of each time step at those cells can be saved in another .ecd file. It is easy to edit those values and get the average over whatever the time range needed. The

restriction of this method is only limited cells can be monitored, which means the plots made out of those values are simple and rough. Figure 3.15 and Figure 3.16 show the results of mass transfer coefficient,

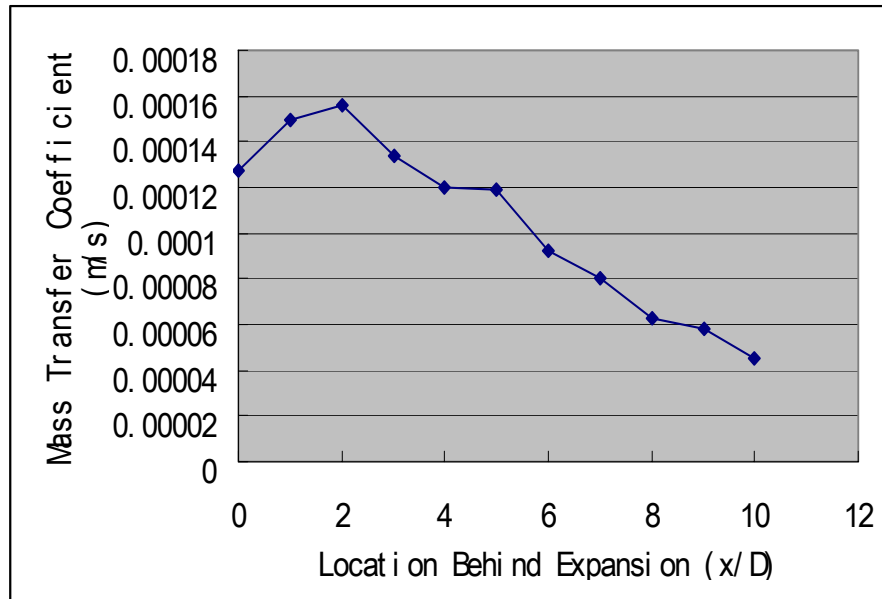


Figure 3.15 Mass transfer coefficient variation at $Re=1,000$

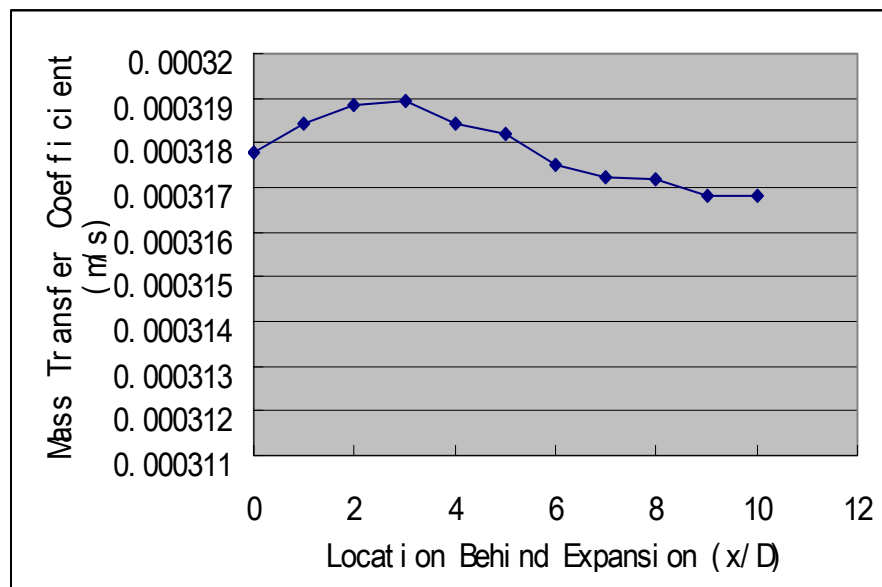


Figure 3.16 Mass transfer coefficient variation at $Re=24,000$

The curve for Reynolds Number of 1,000 appears to be close to the plot obtained using first method, e.g. Figure 3.13. While for Reynolds number of 24,000, Figure 3.16 shows quite a different picture from Figure 3.14. Actually, according to the work from Rizk *et al.* [33], Figure 3.16 provides a better estimation than Figure 3.14, because for higher Reynolds number and more unsteady flow, 10 samples of data is not adequate for even a close approximation.

3.2.3.2 Chemical Kinetics

STAR-CD along with CHEMKIN has been chosen as the tool for analyzing the fluid flow and the chemical reactions that take place. A couple of sections of the Materials Test Loop have been chosen for the analysis purpose. As an approach towards the final problem, a few test cases involving the reaction of lead and oxygen have been considered as a first step. The variations in concentration of oxygen and lead oxide have been closely examined.

Two sections from the MTL have been chosen for the analysis. The first one is the main test section with 1" in diameter and 31.6" in length. Another section is an elbow model with 2" in diameter. The geometries of the two considered sections have been shown in figures 3.17 and 3.18.

Lead and oxygen are allowed to flow through the inlet. The liquid lead reacts with oxygen in both the cases. The velocity, temperature and pressure profiles for both the cases have been depicted. Also, the concentration variations of oxygen and PbO have been shown and the results discussed later. For the above two models, the inlet velocities are taken as 1 m/s and 2.5 m/s respectively. The concentrations of lead and oxygen are

given as 77.5% and 22.5% by weight respectively. An adiabatic wall heat condition has been imposed with the fluid flowing at 823K.

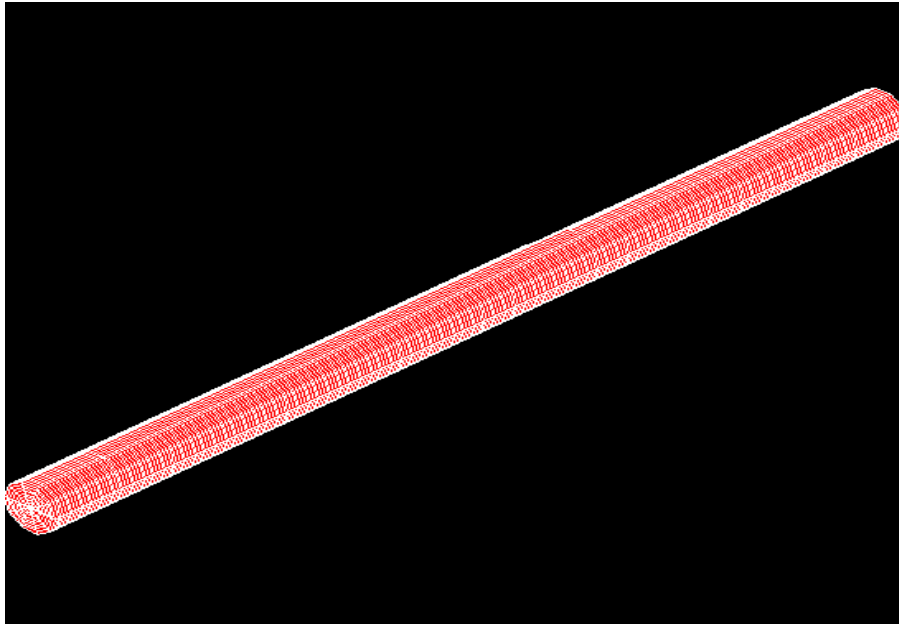


Figure 3.17 Geometric representation of the main test section in the MTL

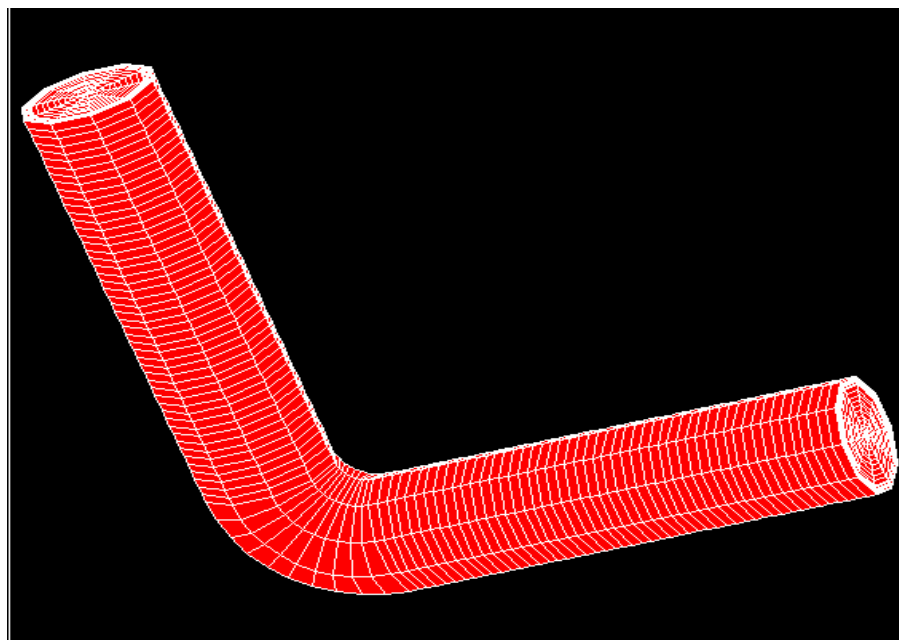


Figure 3.18 Geometrical representation of an elbow section in the MTL

For the straight pipe case, Figure 3.19 shows the velocity profile of the fluids in the pipe section considered. As the flow being considered is laminar, a parabolic profile of the velocity is expected. From the figure, we can see that the average velocity at the outlet is around 1.5 m/s. The results are in complete agreement with the theory showing in a parabolic profile at the outlet.

Figure 3.20 shows the uniform pressure variation along the axial section. The values that can be seen in the picture depict the relative pressures.

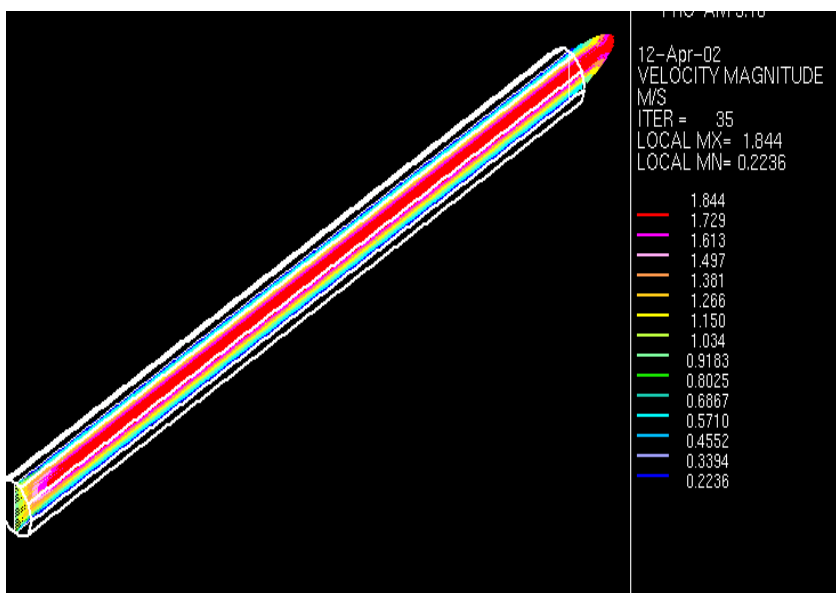


Figure 3.19 Velocity profiles of the fluids along the axial section of the pipe

Figure 3.21 and 3.22 show the concentration of lead oxide, due to reactions between lead and oxygen. The inlet and outlet average concentrations of lead oxide are $0.4771e-13$ and $0.7983e-11$. From the figures, it can be seen that there is a steady increase in the concentration of PbO in the direction of flow. The initial concentration of PbO is zero. When we see the concentration variation more closely at a cross section, it can be observed that concentration at the wall region is higher than the concentration at the

center. This can be seen more clearly from Figure 3.22. This phenomenon may be explained as follows.

As we have seen from the velocity profile, the velocity near to the walls is less than the velocity at the center of the pipe because of the boundary layer theory. So, there is enough time for the reactants to react and hence the concentration at the walls is more than the concentration at the center.

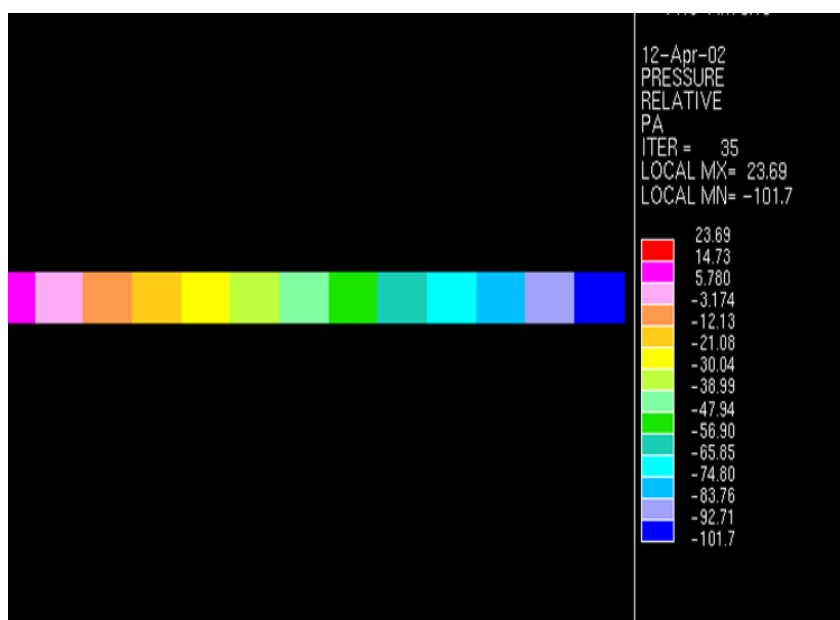


Figure 3.20 Pressure variations along the axial section of the pipe

For the elbow section, the explanation given above also holds good. The things that are of interest might be the velocity profile, pressure profile and the concentration variations. The velocity and pressure profiles in the elbow model are not uniform as in the case of the straight pipe model. This is because of the bend in the pipe. The pipe bend causes a high pressure area near the bend. Because of this the velocity is very low at the bend when compared to the other sections.

Figure 3.23 and 3.24 show the velocity and pressure variations in the elbow model respectively. The average velocity is 3.2 m/s.

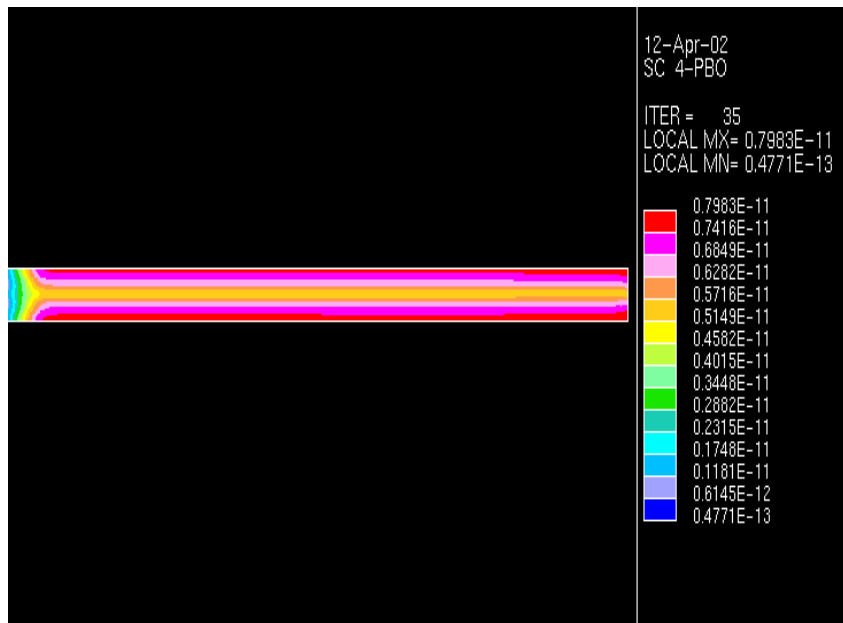


Figure 3.21 Variation of concentration of PbO along the axial pipe section

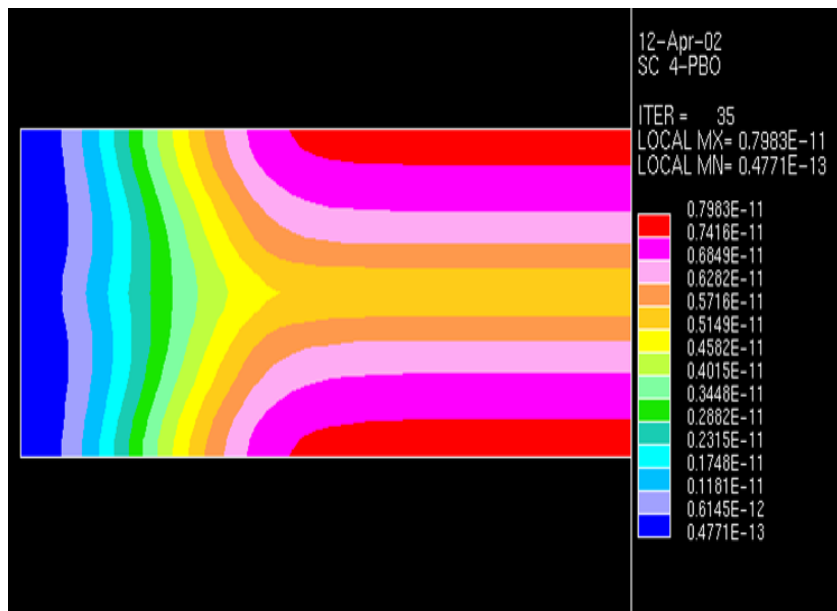


Figure 3.22 Closer view of the concentration variation of PbO

Figure 3.25 and 3.26 show the concentration diagrams of PbO. The first one shows the variation on the surface while the latter one shows the variation along the axial section of the pipe. The concentration varies from 0.2776×10^{-16} at the inlet to 0.1867×10^{-9} . One point may be worth noting here when we compare the elbow model with the previous model. The concentration changes in the lead-oxide in the elbow model seem slower than that in the straight pipe. This has two explanations. First one is that in the elbow model, the fluids are flowing down. Because of this gravitational effects may result. As lead is comparatively a heavier metal, this fluid comes down fast and do not have much time to react with the oxygen. Once it approaches the bend, there is an accumulation of this fluid and so, it has enough time to react with oxygen.

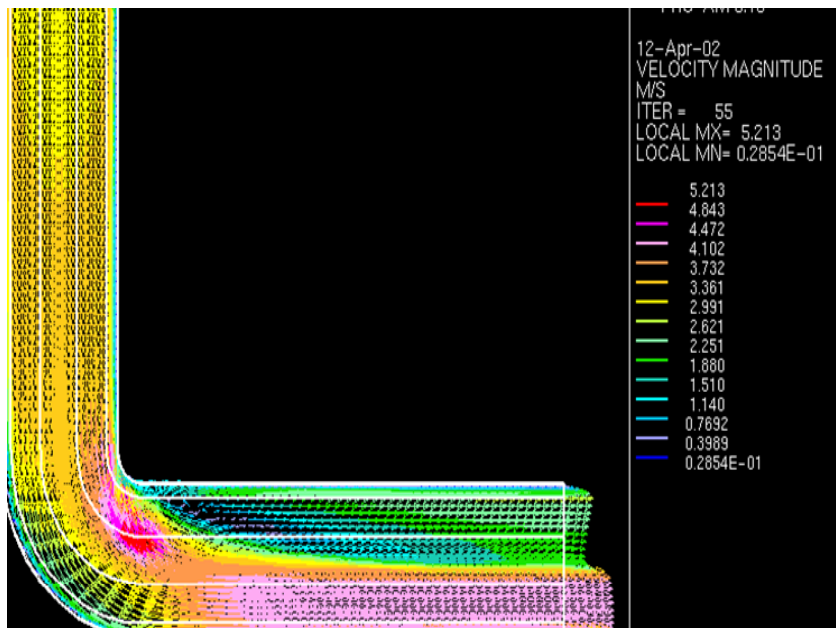


Figure 3.23 Velocity profile along the axial section of the elbow

A steady development can be seen in the concentration from the bend. The second reason for this may be explained by the fact that the length of the pipe in the elbow model is very small when compared to the length of the straight pipe model.

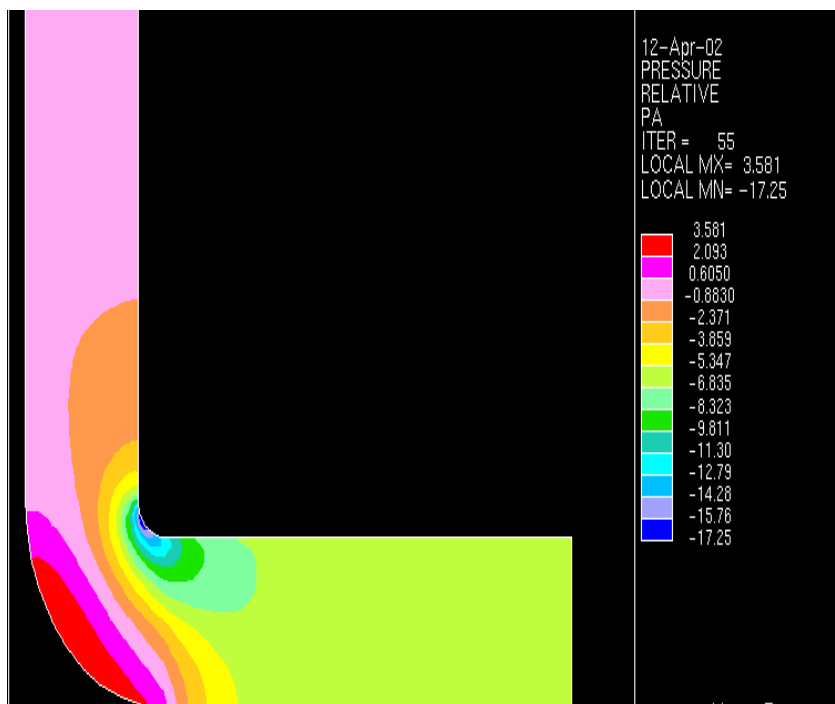


Figure 3.24 Pressure profile along the axial section of the elbow

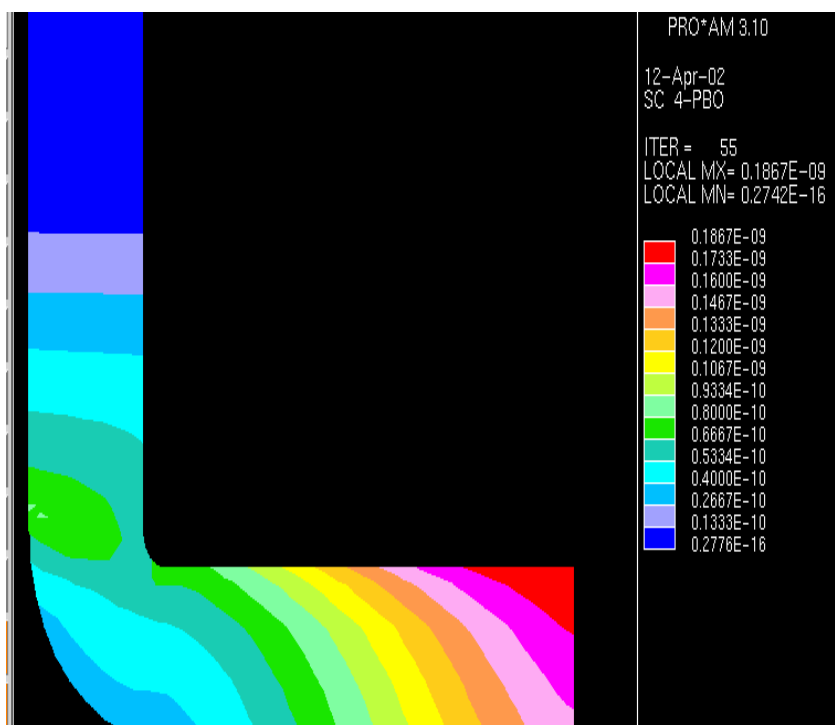


Figure 3.25 Concentration diagram of PbO along the surface of the elbow

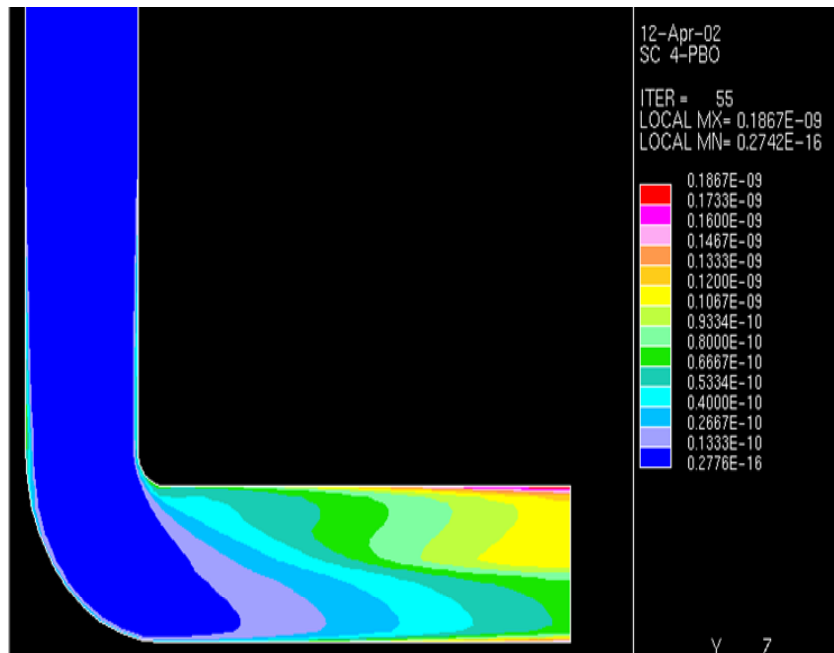


Figure 3.26 Concentration profile of PbO along the axial section of the elbow

CHAPTER IV

CONCLUSIONS AND SUGGESTIONS

Results from self-developed code prove the code works fine. In sudden expansion geometry, mass transfer is affected greatly by expansion ratio, Reynolds Number and physical properties of flow. Expansion ratio does not increase or decrease scale of mass transportation. But it does affect the locations where maximal concentration gradient takes place. Reynolds number and Schmidt number were looked into and found influential to the variation of concentration gradient. Especially, for low Reynolds Numbers around 100, flow phenomenon could be very different, which leads to quite different species transfer performance. As far as Schmidt number is concerned, the order change of it gives rise to the order change of mass transfer, correspondingly.

STAR-CD was applied to achieve the prediction of species transfer in an alternative way. Two methods of analyzing data are introduced. Both of them have their own advantages and disadvantages. And both of them reveal what the trend of mass transfer coefficient looks like, which is something in common for laminar and turbulent flow. It is helpful for the future study on modeling real MTL loop and the prediction the mass transportation in that complicated condition.

In addition, STAR-CD+ CHEMKIN solve the chemical reactions taking place in the flow. Preliminary outcome shows the agreement with physical phenomenon. The reaction

in different geometries, such as straight pipe and elbow, demonstrates reasonable distribution of concentration, which will be a good base for future work.

REFERENCES

1. Nuclear Engineering International, February 2001 (<http://www.world-nuclear.org/education/intro.htm>)
2. Dynamic Analysis of An overhead Crane Carrying A Canister By Finite Element Method –Musukula, University of Nevada, Las Vegas, 1993.
3. <http://apt.lanl.gov/atw/index.html>, (March 21, 2002).
4. Ballinger R.G, Lim J.Y, “Research activities in US related to material compatibility issues for nuclear systems using heavy-liquid-metal coolant,” (2001).
5. Ning Li, Keith Woloshun, Valentina Tcharnotskaria, Tim Darling, Crut Ammerman, Xiaoyi He, Joe King and David Harkleroad, “Lead-Bismuth Eutectic (LBE) Materials Test Loop (MTL) test plan,” (2001).
6. Darling T.W, Ning Li, “Oxygen concentration measurement in liquid Pb-Bi eutectic,” (2001).
7. B.F. Gromov, Yu.S. Belomitcev, E.I. Yefimov, M.P. Leonchuk, P.N. Martinov, Yu. I. Orlov, D.V. Pankratov, Yu. G. Pashkin, G.I. Toshinsky, V.V. Chekunov, B. A. Shmatko, V. S. Stepanov, “ Use of Lead-bismuth coolant in nuclear reactors and accelerator-driven systems,” Nuclear Engineering and Design, 173 (1997) 207-217.
8. J.-L. Courouau, P. Trabuc, G. Laplanche, Ph. Deloffre, P. Taraud, M. Ollivier, R. Adriano, S. Trambaud, “Impurities and oxygen control in Lead alloys,” Journal of Nuclear Materials 301 (2002) 53-59.
9. L. Soler Crespo, F.J. Martín Muñoz, D. Gómez Briceño, “Short-term static corrosion tests in Lead-Bismuth,” Journal of Nuclear Materials 296 (2001) 273-281.

10. Ning Li, "Active control of oxygen in molten Lead-Bismuth Eutectic systems to prevent steel corrosion and coolant contamination," *Journal of Nuclear Materials* 300 (2002) 73-81.
11. F. Balbaud-Célérier, F. Barbier, "Investigation of models to predict the corrosion of steels in flowing liquid Lead alloys," *Journal of Nuclear Materials* 289 (2001) 227-242.
12. "The handbook of fluid dynamics," edit by Richard W. Johnson, Boca Raton, Fla. CRC Press, c1998.
13. "Methodology," STAR-CD User Guide, Version 3.10, 1999
14. A. Acrivos and M. Schrader, "Steady flow in a sudden expansion at high Reynolds numbers," *Phys. Fluids* 25, 923 (1982).
15. F. S. Milos and A. Acrivos, "Steady flow past sudden expansion at large Reynolds number – I. Boundary layer solution," *Phys. Fluids* 29, 1353 (1986).
16. F. S. Milos, A. Acrivos, and J. Kim, "Steady flow past sudden expansion at large Reynolds number – II. Navier-Stokes solution for the cascade expansion," *Phys. Fluids* 30, 7 (1987).
17. E. O. Macagno, and T. K. Hung, "Laminar eddies in a two dimensional conduit expansion," *J. of Fluid Mech.* 28, 43 (1967).
18. O. K. Kwon, R. H. Plethcer, and J. P. Lewis, "Prediction of sudden-expansion flows using the boundary-layer equations," *J. Fluid Eng.* 106, 285 (1984).
19. A. Kumar and K. S. Yajnik, "internal separated flows at large Reynolds numbers," *J. Fluid mech.* 97 27 (1980).

20. T. K. Hung, "Laminar flow in conduit expansions," Ph. D. dissertation, University of Iowa, Iowa City, 1966.
21. H. Morihara, "Numerical integration of the Navier-Stokes equations," Ph. D dissertation, State university of New York at Buffalo, 1972.
22. P. S. Scott, F. A. Mirza, and J. Vlachopoulos, "A finite element analysis of laminar flows through planar and axisymmetric abrupt expansions," *Comput. Fluids* 14,423 (1986).
23. M. Napolitano and P. Cinnela, "A numerical study of planar and axially-symmetric sudden expansion flows," *Comput. Fluids* 17, 185 (1989).
24. D. M. Hawken, P. Townsend, and M. F. Webster, "Numerical simulation of viscous flow in channels with a step," *Comput. Fluids* 20, 59 (1991).
25. A. Baloch, P. Townsend, and M. F. Webster, "On two- and three-dimensional expansion flows," *Comput. Fluids* 24, 863 (1995).
26. F. Durst, A. Melling, and J. H. Whitelaw, "Low Reynolds number flow over a plane symmetric sudden expansion," *J. Fluid Mech.* 64, 111 (1974).
27. W. Chedron, F. Durst, and J. H. Whitelaw, "Asymmetric flows and instabilities in symmetric ducts with sudden expansion," *J. Fluid Mech.* 84, 13 (1978).
28. R. M. Fearn, T. Mullin, and K. A. Cliffe, "Nonlinear flow phenomena in a symmetric sudden expansion," *J. Fluid Mech.* 211, 595 (1990).
29. M. Shapira, D. Degani, and D. Weihs, "Stability and existence of multiple solutions for viscous flow in suddenly enlarged channel," *Comput. Fluids* 18, 239 (1990).
30. D. Drikakis, "Bifurcation phenomena in incompressible sudden expansion flows," *Phys. Fluids* 9, 1 (1997).

31. X. He, N. Li and M. Mineev, "A kinetic model for corrosion and precipitation in non-isothermal LBE flow loop," *Journal of Nuclear Materials* 297 (2001) 214-219.
32. N. K. Ghaddar, K. Z. Korczak and B.B. Mikic, "Numerical investigation of incompressible flow in grooved channel. Part 1. Stability and self-sustained oscillations," *J. Fluid Mech.* 163, 99 (1986).
33. T. Y. Rizk, G. E. Thompson and J. L. Dawson, "Mass transfer enhancement associated with sudden flow expansion, " *Corrosion Science*, Vol. 38, No. 10, (1996).

VITA

Graduate College
University of Nevada, Las Vegas

Chao Wu

Local Address:

1600 East University Avenue #211
Las Vegas, NV 89119

Home Address:

Xikang Road 1-8, Room 806
Nanjing, 210024
China

Degrees:

Bachelor of Science, Materials Science and Engineering, 2001
Southeast University

Thesis Title: Study of Geometry Effects on Local Corrosion Rates for LBE Loop

Thesis Examination Committee:

Chairperson, Dr. Yitung Chen, Ph.D.
Chairperson, Dr. Samir Moujaes, Ph.D.
Committee Member, Dr. Darrell W. Pepper, Ph.D.
Committee Member, Dr. William Cullbreth, Ph.D.
Committee Member, Dr. Jichun Li, Ph.D.